









RESEARCH ARTICLE

Temperature-dependent electromechanical response of $\text{BaTi}_{1-x}\text{Sn}_x\text{O}_3$: Analysis of reversible and irreversible contributions

Viktoria Kraft¹  | Udo R Eckstein¹  | Michel Kuhfuß¹  |
Neamul H Khansur^{1,2}  | Frederick P Marlton³  | Bryce Mullens⁴  |
Alexander Martin⁵  | Koichi Hayashi⁶  | Kyle G Webber¹ 

¹Department of Materials Science and Engineering,
Friedrich-Alexander-Universität
Erlangen-Nürnberg, Erlangen, Germany

²Department of Materials Science & Engineering, Case Western Reserve University, Cleveland, Ohio, USA

³School of Mathematical and Physical Sciences, University of Technology Sydney, Ultimo, New South Wales, Australia

⁴School of Chemistry, University of Sydney, Sydney, New South Wales, Australia

⁵Department of Life Science and Applied Chemistry, Nagoya Institute of Technology, Nagoya, Japan

⁶Department of Physical Science and Engineering, Nagoya Institute of Technology, Nagoya, Japan

Correspondence

Viktoria Kraft, Department of Materials Science and Engineering,
Friedrich-Alexander-Universität
Erlangen-Nürnberg, Erlangen 91058,
Germany.
Email: viktoria.kraft@fau.de

Funding information

Deutsche Forschungsgemeinschaft,
Grant/Award Number: GRK2495/F/H/S

Abstract

The increasing demand for efficient, multifunctional energy conversion systems has sparked interest in light-active polar perovskite oxides. These materials offer structural flexibility and chemical tunability, making them promising candidates for multimodal energy harvesting. In particular, photoferroelectrics enable the simultaneous harvesting of thermal, light, and mechanical energy. However, mostly room temperature properties have been studied, leaving a critical gap in understanding their behavior under varying thermal conditions. This study investigates the electromechanical properties in conjunction with crystallographic changes of photoferroelectric $\text{BaTi}_{1-x}\text{Sn}_x\text{O}_3$ across a temperature range of -150°C to 150°C . Increasing Sn content reduces tetragonal distortion, shifts phase transition temperatures, and induces a multi-phase region at higher concentrations. As a result, temperature-dependent small-signal measurements show changes in dielectric and piezoelectric responses, with a trend toward relaxor-like behavior at higher Sn levels. Rayleigh analysis of stress amplitude-dependent piezoelectric coefficient reveals enhanced properties at specific compositions, for example, 7 mol% Sn) and temperatures, attributed to an optimal balance of reversible and irreversible contributions. Further, Sn doping appears to improve thermal stability by reducing irreversible contributions. These results provide significant implications for optimizing photoferroelectric BaTiO_3 by influencing material properties through Sn doping for various applications, including energy harvesting.

KEYWORDS

barium titanate, electromechanical properties, ferroelectricity/ferroelectric materials, low temperature, piezoelectric materials/properties

This is an open access article under the terms of the [Creative Commons Attribution](https://creativecommons.org/licenses/by/4.0/) License, which permits use, distribution and reproduction in any medium, provided the original work is properly cited.

© 2025 The Author(s). *Journal of the American Ceramic Society* published by Wiley Periodicals LLC on behalf of American Ceramic Society.

1 | INTRODUCTION

The conversion of energy is critical in energy harvesting and storage systems, where light (photovoltaic,¹ photocatalytic,² photoferroelectric effect³), strain gradients (flexoelectric effect⁴), stress (piezoelectric effect⁵), thermal fields (pyroelectric effect⁶), magnetic fields (magnetoelectric effect⁷), and chemical energy (electrochemical conversion⁸), among others, can be converted into usable electrical power, thereby serving as the foundation for numerous technological applications. To widen the range of applications beyond single-function implementations, multimodal energy conversion systems, capable of simultaneously converting energy from multiple sources, offer enhanced versatility by integrating various energy forms into a single device.⁹ This capability gives rise to multisource phenomena, such as the piezophotonic effect,¹⁰ that is, photonic excitation via piezoelectric polarization, photostriction,¹¹ that is, light-induced deformation through internal electric fields, and multiferroic,¹² that is, a combination of ferroelectric, ferroelastic, and ferromagnetic properties, to name a few. It should be noted that several materials have the ability to convert energy from multiple sources by themselves, without additional device design, making them strong candidates for multimodal energy conversion. Potassium sodium barium nickel niobates ($[\text{K}_{1-x}\text{Na}_x\text{NbO}_3]_{1-y}[\text{BaNi}_{1/2}\text{Nb}_{1/2}\text{O}_{3-\delta}]_y$, K(N)BNNO) are such candidates due to their piezoelectric–pyroelectric–photovoltaic properties.^{13–15} As a result, KBNNO samples have demonstrated increased electrical power output density of around $0.5 \mu\text{W} \cdot \text{cm}^{-3}$ for energy harvesting applications by converting multiple forms of energy, such as mechanical vibrations, heat, and light simultaneously, rather than functioning solely as a vibration energy harvester (power density of approximately $0.15 \mu\text{W} \cdot \text{cm}^{-3}$).¹⁶ Another notable candidate is BiFeO_3 , a multiferroic material¹⁷ that also exhibits antiferromagnetic behavior,¹⁸ changing its magnetic properties by an applied electrical and/or mechanical field. In addition, BiFeO_3 is also photoferroelectric,¹⁹ combining photosensitivity with ferroelectric properties and possessing a band gap of 2.2–2.7 eV,^{13,20} which can be further reduced by doping.²¹ Another exciting material that exhibits photoferroelectric properties is BaTiO_3 ; its coupled²² and individual properties²³ have been studied extensively. While photoferroelectrics are an intriguing class of materials with coupled functionalities, from a purely photovoltaic standpoint, these materials face challenges, including low photovoltage, quantum efficiency, and insufficient bulk conductivity.²⁴ Nevertheless, photoferroelectrics are noteworthy for features such as above-bandgap

open-circuit voltage (V_{OC}), the contribution of internal electric fields to charge carrier separation, and enhanced photovoltage, among others.²⁴ However, it is important to note that the role of domains and domain wall mobility is critical in photoferroelectrics, in particular near phase boundaries.^{25,26} Despite the potential applications for this emerging class of materials, there remains little information about the temperature-dependent electromechanical response of photoferroelectric materials, which is critical for fully utilizing their multimodal energy conversion properties.

BaTiO_3 is an excellent model material for chemically tuning photoferroelectric properties. In addition to being extensively studied since its discovery in the 1940s, more recent investigations have shown that photoferroelectric properties can be observed through chemical substitutions.^{27,28} In this material system, it is well-established that doping and substitution can change the crystal structure and phase boundaries and, by extension, tune and enhance ferroelectric properties. Significant efforts have been made in the chemical engineering of the A-site (isovalent: Sr^{2+} , Ca^{2+} aliovalent: La^{3+} , Pr^{3+}) and B-site (isovalent: Zr^{4+} , Ce^{4+} aliovalent: Nb^{5+}), as well as the combinations of both.^{29,30} These modifications have an impact on fundamental characteristics, such as the microstructure^{31–33} and crystal structure,^{32,34} which changes from rhombohedral to cubic with increasing Ca^{2+} doping.³² They also affect phase boundaries and phase coexistence regions,^{23,29} shift the transition temperatures either to higher or lower values depending on the doping site and type, and influence the polymorphic/morphotropic phase boundaries, as observed for instance in $(\text{Ba}_y\text{Ca}_{1-y})(\text{Zr}_x\text{Ti}_{1-x})\text{O}_3$.^{23,35,36} Consequently, these changes alter the overall ferroelectric response,^{30,37} such as increasing the remanent polarization for Al^{3+} doping.³⁸ Additionally, doping and substitution can have an impact on the photosensitivity of the material by changing properties such as the band gap,^{27,39,40} for instance, reducing it from around 3.2 to 2.42 eV with the addition of Co^{2+} .⁴¹

One of the more promising dopants for enhancing photoferroelectricity in BaTiO_3 is Sn. Sn doping not only modifies the band gap,³⁹ but also changes photoconductivity and current.²⁷ Additionally, Sn doping has a profound impact on the electromechanical properties,^{42–49} which have been extensively characterized, mostly concentration-dependent, but with significant deviations in the results, depending on the characterized properties. Although there is agreement between dielectric measurements and the resulting phase diagram,^{44,48,50–53} deviations are reported in the microstructure,^{43,46,47,49,50,54} ferroelectric,^{43,45,47,49,50,54–60}

and piezoelectric properties,^{42–50} to name a few, even though characterized for the same Sn-content. Temperature-dependent observations of the ferroelectric and piezoelectric properties could reveal if these deviations are due to slight variations in the phase transition temperatures and measurement temperature or other underlying phenomena. Therefore, it is crucial to analyze trends over a broader temperature range to gain a better understanding of how Sn-content influences the electromechanical response. Bridging the knowledge gap in the low-temperature range of electromechanical properties—encompassing structural, dielectric, piezoelectric, and ferroelectric properties—is essential to understanding their impact on coupled functionalities.⁶¹ As such, the small signal dielectric and piezoelectric responses, as well as the large field ferroelectric hysteresis, were characterized as a function of temperature across the rhombohedral, orthorhombic, tetragonal, and cubic phases. By recording the frequency- and stress-amplitude-dependent electromechanical response, the temperature-dependent domain wall mobility, as well as the reversible and irreversible contributions, could be determined. These data are discussed in conjunction with temperature-dependent crystal structures determined using high-resolution powder X-ray diffraction from -100°C to 150°C . By understanding the material system behavior, not only as a function of Sn concentration but also over a broad temperature range, valuable insights are gained for the future design of further Sn-doped photoferroelectric BaTiO_3 materials.

2 | EXPERIMENTAL METHODOLOGY

Polycrystalline $\text{BaSn}_x\text{Ti}_{1-x}\text{O}_3$ ($x = 0, 0.03, 0.05, 0.07, 0.09, 0.11, 0.13, 0.15$) ($\text{BTSn}100x$, $0 \leq x \leq 0.15$) samples were prepared by the solid-state synthesis reaction method using analytical grade starting materials: BaCO_3 (99.8% purity, Thermo Fisher Scientific), SnO_2 (99.9% purity, Thermo Fisher Scientific), and TiO_2 (99.6% purity, Thermo Fisher Scientific). To ensure stoichiometric weighing, the powders were dried overnight at 120°C , and a humidity-controlled glove box ($\text{RH} < 15\%$) was used. This was followed by ball milling in ethanol (EtOH) for 24 h to homogenize. The powders were dried by removing the EtOH under reduced pressure with a rotary evaporator. Subsequently, the powders were calcined at 1200°C for 6 h (5 K/min cooling and heating rate) using an alumina crucible. To achieve homogeneous and fine particle size, the powders were ball milled for 72 h, dried, and sieved (100 μm mesh). The final powders were stored in an oven at 120°C , were uniaxially pressed into disks and cylinders with a diameter of 10.2 and 8.2 mm, respectively. Further

densification was achieved by means of cold isostatic pressing for 5 min at 180 MPa, and sintering at 1380°C for 4 h (5 K/min cooling and heating rate). With a surface grinder, disk samples with a diameter of 8.4 mm (± 0.1 mm) and a thickness of 0.8 mm (± 0.02 mm) and cylindrical samples with a diameter of 5.8 mm (± 0.02 mm) and a height of 6 mm (± 0.02 mm) were processed. To release internal residual stress induced by grinding, the samples were annealed at 400°C for 4 h. For small signal electromechanical and ferroelectric characterization, Pt electrodes (Q 150T S plus, Quantum Design) were sputtered on opposing parallel surfaces of the samples with an approximate thickness of around 100–200 nm.

A scanning electron microscope (SEM, Helios Nano-Lab 600i FIB Workstation, FEI Company) was used to take microstructural images of seven different spots on each sintered body. The grain size was analyzed using a commercially available, automated image evaluation software (MIPAR v5.0 with Spotlight Package, MIPAR Image Analysis, USA), with at least 350 grains per composition. Prior to the measurement, the samples were ground to a thickness of 450 μm , mirror polished, and thermally etched at 1200°C for 5 min. The density was measured using Archimedes' method, revealing a relative density above 95% (Table S1).

At the Australian Synchrotron, SXRD (Synchrotron X-ray diffraction) data were collected on a powder diffractometer BL-10 using 21.0 keV photons. The accurate wavelength of the X-rays ($\lambda = 0.5904 \text{ \AA}$) and the Thompson-Cox-Hastings instrument resolution function were obtained through Rietveld refinement of the LaB6 (NIST SRM660B) standard.⁶² As sample holders, 0.2 mm borosilicate glass capillaries were used. Each capillary was rotated during data collection to reduce preferred orientation effects. Temperature control was maintained with an Oxford Cryosystems Cryostream. Data collection utilized an array of 16 Mythen II microstrip detector modules. To bridge the gap between individual modules, two data sets were gathered with the detector assembly shifted by 0.5° .

A custom-built measurement setup was used to record temperature-dependent small signal electromechanical properties as a function of frequency and loading amplitude. A screw-driven load frame (5967, Instron) with an integrated thermal chamber (TK 26.600.LN2, Fresenberger GmbH) using liquid nitrogen enables measuring temperature-dependent capacitance (0.1 kHz–1 MHz) and piezoelectric charge coefficient (0.5–140 Hz) from -150°C to 150°C (2 K/min heating and cooling rate) via electrical connections to an LCR meter (E4980AL, Keysight). The cylindrical samples were placed inside the heating chamber between tungsten carbide electrical contacts using a preload of 5 MPa required for maintaining electrical contact. The piezoelectric actuator (P-025.80, PI Ceramics GmbH) applied a stress amplitude of ± 0.5 MPa. The

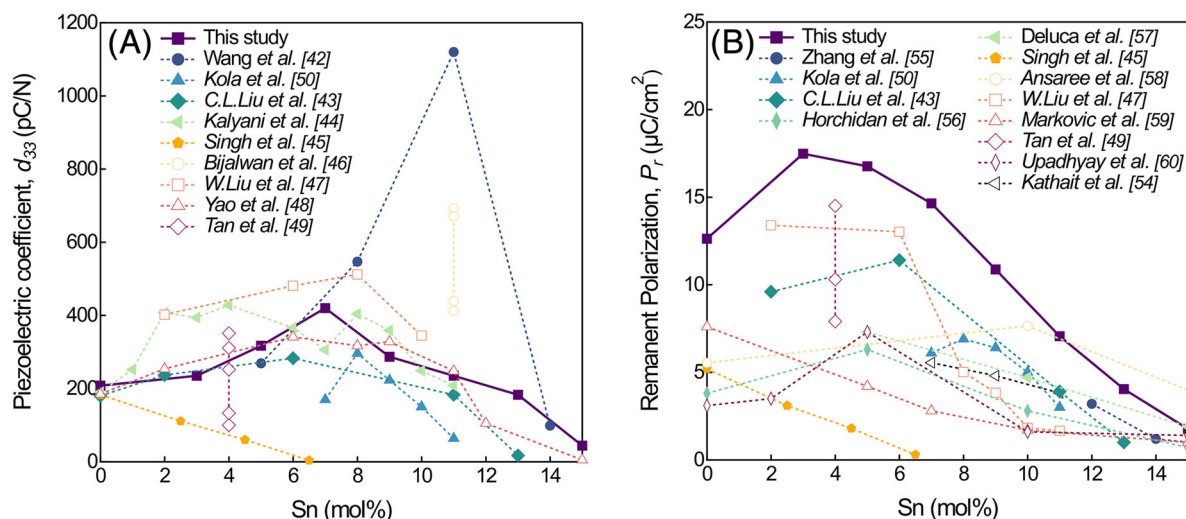


FIGURE 1 Sn-doped BaTiO₃ room temperature (A) piezoelectric coefficient with reported values,^{42–50} and (B) remanent polarization with reported values^{43,45,47,49,50,54–60} Sn concentration dependent.

detailed design of the setup has been documented in previous publications.^{63,64} The cylindrical samples were poled with an electric field of 2 kV/mm for 10 min in a silicone oil bath at room temperature before the measurement. Temperature-dependent Rayleigh analysis was performed using this setup by measuring the piezoelectric charge coefficient at 10 Hz from -150°C to 150°C (2 K/min heating and cooling rate) as a function of stress amplitude (± 0.5 to ± 3 MPa). Therefore, the stress preload needed to be increased to 8 MPa during this measurement to maintain electrical contact.

Temperature-dependent ferroelectric polarization–electric field hysteresis loops were measured from -125°C to 125°C using a commercially available piezoelectric analysis system (TFAnalyzer 2000, aixACCT Systems GmbH). The disk samples were measured at 10 Hz and an electric field of 2 kV/mm with a high-voltage power amplifier (Model 20/20C, Trek), applying a bipolar triangular waveform.

3 | RESULTS AND DISCUSSION

3.1 | Room-temperature material behavior

Room-temperature (RT) investigations are often the starting point for studying material behavior, although this approach can be insufficient. Figure 1 compares literature-reported RT piezoelectric and ferroelectric responses of BTSn100x ($\text{BaSn}_x\text{Ti}_{1-x}\text{O}_3$, $0 \leq x \leq 0.15$) with varying Sn content, revealing significant deviations between studies. The measured samples (BT, BTSn3, BTSn5, BTSn9, BTSn11, BTSn13, and BTSn15, of 208, 235, 317, 287, 235,

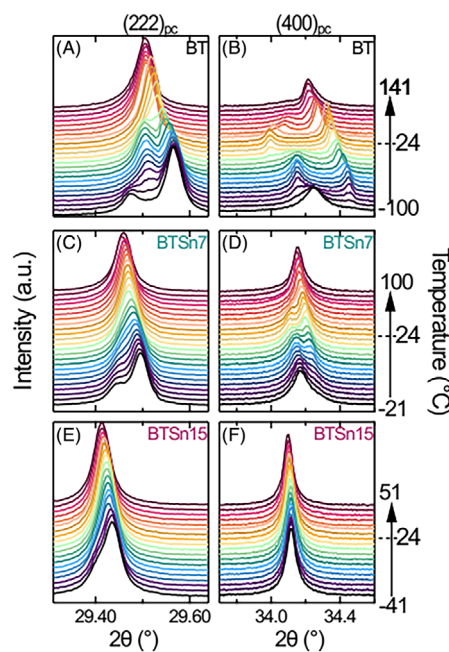


FIGURE 2 Temperature-dependent variation in crystal structure of (A, B) BT, (C, D) BTSn7, and (E, F) BTSn15.

183, and 44 pC/N, respectively) show a maximum of the piezoelectric coefficient d_{33} around 420 pC/N at 7 mol% of Sn doping (Figure 1A), which could occur due to the coexistence of phases at ambient temperature as observed in the XRD data (Figure 2). In contrast, Singh et al.⁴⁵ reported a minimum of around 4 pC/N at a similar concentration of 6.5 mol% Sn. Further, Wang et al.⁴² observed their maximum of approximately 1120 pC/N at an even higher concentration of 11 mol% Sn doping. Similarly, the reported remanent polarization P_r values show significant variations. Figure 1B shows an initial increase for

BTSn3 at RT, consistent with other studies reporting a similar trend for low Sn concentrations (around 6 mol%).^{43,56,60} The observed lower P_r in BT compared with Sn-doped samples may result from increased grain size⁶⁰ or proximity to a structural phase transition at RT. Most studies report an overall linear decrease in polarization with increasing Sn content.^{45,50,59}

In general, it should be noted that the strong deviation in both d_{33} and P_r could be attributed to the processing parameters. Importantly, the previously reported materials have been prepared using different calcination and sintering temperatures,^{45,46,48–50,55–57} different holding times and temperature profiles,^{44,50} additional binders for higher densification,^{45–47,50} inclusion of MnO₂ for conductivity reduction,⁴² different homogenization and milling procedures,^{43–45} as well as different pressing techniques or sample molding, for example, via 3-D printing.⁴³ All these changes in the sample production can lead to different properties of the final samples; for instance, apparent crystal structure, vicinity to a phase boundary, domain type, domain size, microstructure, i.e., relative density and grain size, as well as defects and vacancies, which all influence the overall electromechanical behavior.²³ The measured d_{50} grain size, representative images shown in Figure S1, is more than halved by Sn doping (around 26 μm) compared with BT (around 56 μm), without a clear trend among Sn-doped samples (Figure S2). Reports on grain size also show significant variation, with most stating a reduction in grain size with increasing Sn content,^{43,47,50,53,54,65–67} while some nano-powder studies suggest the opposite^{45,68} (Figure S3A). BT is known to have an optimal grain size for maximizing d_{33} (about 1 μm) and an increase in P_r with grain growth until saturation is reached.⁶⁹ While a similar trend may exist in Sn-doped samples, the current data are insufficient to confirm this (Figure S3B,C). The measured apparent density (Tab. S1) increased with higher Sn content, aligning with some studies,^{50,54} while others report the opposite trend^{45,68} (Figure S4A). As generally expected, a higher apparent density improves functional properties; however, no clear correlation between d_{33} or P_r and density alone is observed for Sn-doped samples (Figure S4B,C). Beyond processing conditions, measurement parameters such as applied electrical and mechanical fields, as well as measurement frequency, amongst others, must also be considered as sources of deviation in reported RT properties.^{61,70} Additionally, the sample history plays a significant role, as differences arise depending on whether a virgin sample or one subjected to temperature, electric field, or others is analyzed.^{19,61,70–72} Therefore, focusing solely on Sn-dependent room-temperature measurements is insufficient for understanding material behavior and leads to significant deviations, as demonstrated above. To gain deeper insight into the impact of Sn on the elec-

tromechanical properties of BT, temperature-dependent studies were conducted across a wide composition range under consistent conditions. The effects of crystal structure, phase transitions, and reversible and irreversible contributions to the material response were examined, while considering the material history, as detailed below.

3.2 | Temperature-dependent structure characterization

To understand the composition-dependent variation in phase transition temperatures, in situ temperature-dependent high-resolution powder XRD data were collected for all Sn-doped compositions at the Powder Diffraction beamline of the Australian Synchrotron.⁶² The temperature range was selected to span from the lowest symmetry rhombohedral (R) phase to the highest symmetry cubic (C) phase. Figure 2 shows the evolution of pseudo-cubic (222)_{pc} and (400)_{pc} reflections as a function of temperature for BT, BTSn7, and BTSn15. The full recorded reflection patterns are shown in Figure S5A,B. Qualitative observation reveals a (222)_{pc} doublet and a single (400)_{pc} reflection at the lowest temperature phase, that is, stabilization of R phases with different extents of crystal distortion. Moreover, the variation in phase transition temperature is also apparent from these data. Importantly, BTSn7 shows the phase coexistence around ambient temperature, that is, 24°C. Coexisting phases can be beneficial to enhance the electromechanical properties.

The temperature-dependent XRD measurements were used to evaluate the phase composition. It should be noted that the phase transition temperatures of undoped BT also depend on extrinsic factors, such as grain size and defects.^{73,74} At temperatures above the Curie point ($T > 127^\circ\text{C}$), the material is cubic. Upon cooling, the tetragonal phase appears below the Curie point, transitioning to the orthorhombic phase around 5°C, which persists down to approximately -90°C . Below this, undoped BT exhibits a rhombohedral phase. These transitions can be represented as follows: $\text{C} \xrightarrow{\approx 127^\circ\text{C}} \text{T} \xrightarrow{\approx 5^\circ\text{C}} \text{O} \xrightarrow{\approx -90^\circ\text{C}} \text{R}$ (T: tetragonal, O: orthorhombic).⁷⁵ Figure 3 shows the (222)_{pc} and (400)_{pc} reflections at 24°C (ambient temperature) and at -100°C as a function of Sn concentration between 3 mol% and 15 mol%. As can be seen in Figure 3A–C, increasing Sn concentration decreases the tetragonal distortion of the parent BT composition and becomes insignificant for Sn concentrations ≥ 9 mol%. However, the split and asymmetric (222)_{pc} reflections for $\text{Sn} \leq 0.09$ indicate the coexistence of multiple lower symmetry phases in this compositional range.⁷⁶ The increased Sn-concentration above 9 mol% stabilizes the cubic phase around ambient temperature, as indicated by the single symmetric (222)_{pc}

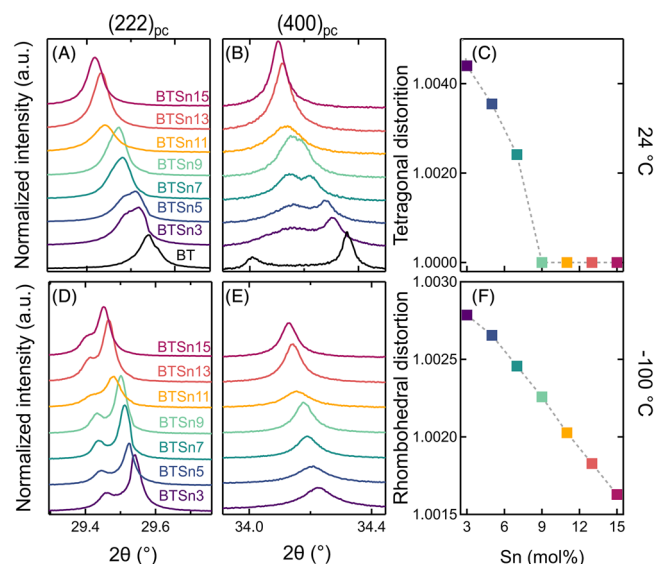


FIGURE 3 Influence of Sn doping on the crystal structure (A–C) at 24°C and (D–F) at –100°C. BT is shown for reference at 24°C, indicating tetragonal distortion with $c/a \approx 1.0096$.

and (400)_{pc} reflections. It is important to note that the diffraction data presented here provide information on the average crystal structure, where the existence of local-scale polar distortion for compositions with higher Sn concentrations at 24°C cannot be ignored.⁴² It is also apparent that the replacement of Ti^{4+} (0.605 Å) with Sn^{4+} (0.69 Å) tends to shift the peak position toward a lower 2θ angle, indicating an increase in d-spacing. Moreover, no additional minor reflections (Figure 2; Figure S5A) were apparent with increasing Sn doping, highlighting the solid solution formation without any secondary phase. At –100°C, the lower symmetry R phase of parent BT is also influenced by the Sn content (Figure 3D–F). The increased Sn content decreases the rhombohedral distortion linearly from 1.0028 to 1.0016, that is, a decrease of 0.12% for 12 mol% of Sn addition, indicating that approximately 30 mol% of Sn will eliminate the rhombohedral distortion at –100°C. With increasing Sn content, reduced T and R distortions are expected to diminish the reversible contributions to the piezoelectric coefficient due to increased crystal symmetry, as discussed below.

3.3 | Temperature-dependent small signal electromechanical properties

To investigate the role of Sn content on the small signal (sub-coercive-field) electromechanical properties, temperature- and frequency-dependent piezoelectric coefficient (d_{33}) and dielectric (ϵ_r) properties were characterized across the phase boundaries (Figure 4). Clear anoma-

lies in both the small signal piezoelectric and dielectric responses were observed for the different compositions, which indicate a structural phase transition. In Figure 4A, the evolution of the phase transitions with increasing Sn content in the dielectric data from –150°C to 150°C and 100 Hz to 1 MHz is shown. The visible phase transitions clearly indicate the presence of the four crystallographic phases of BT: rhombohedral (R), orthorhombic (O), tetragonal (T), and cubic (C). With the addition of Sn, the transition temperatures of the lower symmetry phases (R–O and O–T) increase toward higher temperatures, while the ferroelectric–paraelectric transition to the high symmetry phase (T–C) occurs at decreasing temperatures. In other words, the Curie point (T_C) decreases below RT while the R-phase content increases, which has been previously observed for isovalent B-site doping.^{51,77–79} As such, for BT, BTSn3, BTSn5, and BTSn7, three phase transition temperatures during heating from R to O (T_{RO}) at –64, –14, 8, and 24°C, from O to T (T_{OT}) at 23°C, 38°C, 46°C, and 46°C, and from T to C (T_C) at 130°C, 105°C, 90°C, and 72°C were observed, respectively. A coexistence region is observed above 9 mol% Sn. For BTSn9, BTSn11, BTSn13, and BTSn15, a ferroelectric–paraelectric phase transition is represented as one dielectric anomaly in the temperature-dependent data and was found at 57, 41, 27, and 10°C, respectively. The evolution of the different phases was already discussed in relation to the XRD data (Figure 3), which shows clear evidence of a reduction of tetragonal distortion with higher Sn content at room temperature. Frequency dispersion in the relative permittivity is mostly visible for BT–BTSn7 between –60°C in the R phase until the respective T_C , and is especially pronounced in the vicinity of the observed structural phase transitions (Figure S6). The loss of dispersion at even lower temperatures is likely due to the freezing of extrinsic contributions, such as defects, oxygen vacancies, etc.⁸⁰ As the temperature increases, charge carriers become more mobile, although this does not directly affect the polarization response.⁵² In addition to defects, domain wall mobility has been shown to have a freezing effect below room temperature, which could have a direct impact on the electromechanical response through a reduction in the extrinsic contributions.⁸¹ In addition, the samples BTSn9–15 show a small, less pronounced onset of dispersion in the R phase toward the transition to the C phase, which is diminished after the transition.

The ferroelectric–paraelectric phase transition region was examined by determining the temperature at maximum permittivity (T_m) as well as the Curie–Weiss temperature (T_0) (Figure S7A,B).⁸² The deviation $T_m - T_0$ is positive for a first-order phase transition (Figure S7A), where the first derivative of the order parameter, the spontaneous polarization, is discontinuous. For a second-order phase transition, the first derivative is continuous,

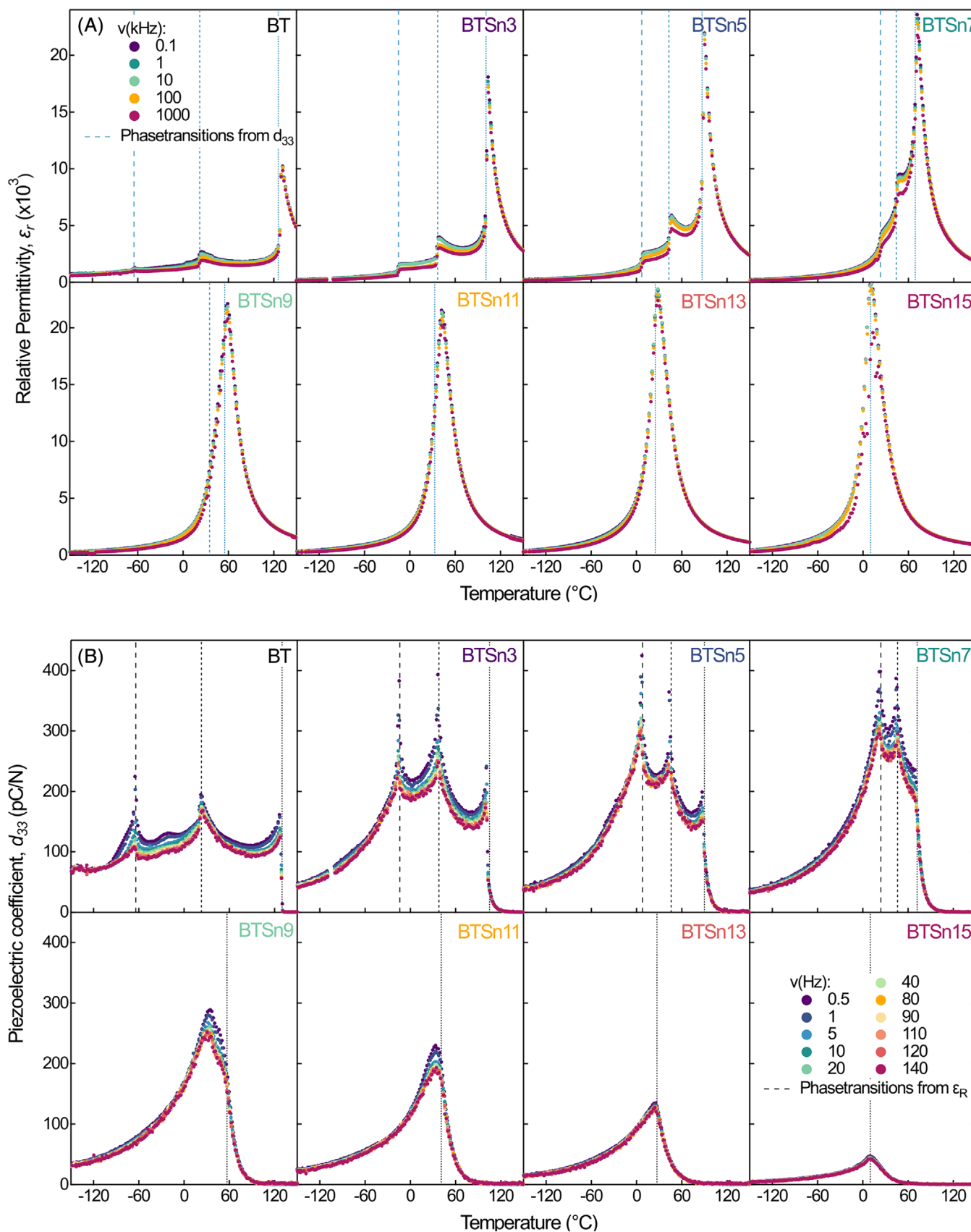


FIGURE 4 Temperature-dependent characterization of (A) rel. permittivity between 0.1 kHz and 1 MHz with phase transition temperatures from the piezoelectric measurement (light blue lines) and (B) piezoelectric coefficient between 0.5 and 140 Hz with dielectric phase transition temperatures (black lines).

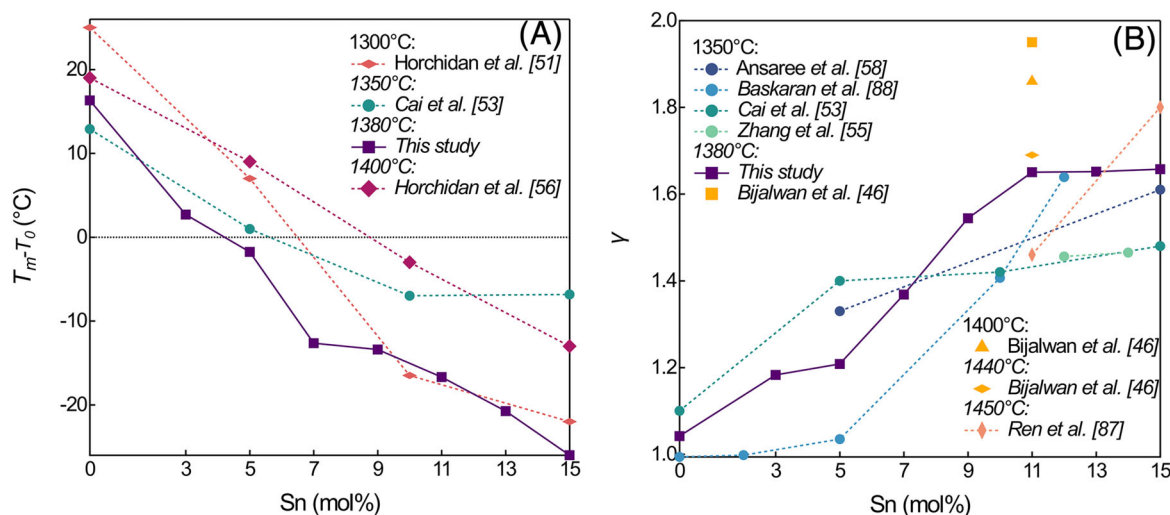


FIGURE 5 Sn concentration-dependent comparison of (A) the difference between T_m and T_0 with previous reports,^{51,53,56} and (B) the derived gamma value γ with previous reports^{46,53,55,58,87,88} to analyze the phase transition.

and $T_m - T_0$ becomes 0. Since relaxors do not follow the Curie–Weiss law, T_0 is difficult to determine; however, when attempting to define T_0 for relaxor-like systems, the deviation $T_m - T_0$ becomes negative. Accordingly, with increasing Sn-content, the deviation decreases (Figure 5A), indicating a change from a 1st order phase transition, as reported for BT,^{5,83} toward a “relaxor phase transition” as described by Damjanovic.⁸⁴ This behavior is also observed in relaxor-like systems exhibiting dielectric relaxation into the paraelectric phase.^{52,55,56,78,85,86} Another indication for this change can be found in the diffuseness factor γ (Figure 5B; Figure S9), where the modified Curie–Weiss law increases with higher Sn-content from 1.042 to 1.6573 for BT to BTSn15, respectively, indicating greater diffuseness in the ferroelectric-to-paraelectric transition. Moreover, a sharp increase in the maximum relative permittivity value at T_C is visible by doping with Sn in comparison to pure BT; for instance, BTSn15 has a maximum ϵ_r of around 24 000 at T_C , while BT only shows 10 000. The light blue lines indicate the depolarization temperature T_d , defined here using the local piezoelectric maxima close to T_C , and above 5 mol% Sn via the intercept of two linear fits (Figure 4B). These lines are mostly located around the inflection points preceding the dielectric anomaly maxima, meaning they are lower in temperature than the T_C derived from the maxima of the dielectric data. This trend is more apparent in Figure S10A, which shows overall lower T_d values for all the compositions. A general decrease in both the T_d and T_C with increasing Sn content can be observed. Figure S10A also contains the temperature at which the d_{33} drops below 2 pC/N, denoted as T_{d^*} , which is used here to define the point of most depolarization. Interestingly, this temperature decreases with increasing Sn-content at a rate of approx-

imately $-4^\circ\text{C}/\text{mol}\%$, which is slower than the decrease observed for T_d and T_C , both around $-8^\circ\text{C}/\text{mol}\%$. Furthermore, it is known that electromechanical properties strongly increase toward phase boundaries, as described below.

In Figure 4B, the direct d_{33} is shown from -150 to 150°C for 0.5–140 Hz to determine the temperature stability and operation range for different compositions. The same crystallographic phases, transitions, and coexistence regions are observed for the different compositions as in Figure 4A. As is apparent in Figure 4B, three clear peaks in the piezoelectric response are found in BT, corresponding to the three known phase transitions previously discussed. With an increasing Sn content, there is an initial increase in the d_{33} values at temperatures above -60°C as well as an apparent shifting of the phase boundaries, similar to that found in the dielectric response (Figure 4A). However, for Sn concentrations above about 7 mol%, the phase boundaries begin to overlap and distinct d_{33} peaks are no longer visible, which might be due to the formation of a phase coexistence region.^{42,44,47,48} Importantly, the d_{33} highly depends on the measuring frequency, where low frequencies, such as 0.5 Hz, show especially high values around phase boundaries. For Sn concentrations up to 11 mol%, the frequency-dispersion occurs in the vicinity of the phase transitions, where variations are due to the changes in the thermal activation of the extrinsic contributions, that is, domain wall motion (Figure S8). Here, defects, such as oxygen vacancies⁸⁹ as well as domain wall pinning⁹⁰ and displacement,⁷¹ among others, are particularly important. However, for the highest Sn contents of 13 and 15 mol%, there is an apparent reduction in the frequency dispersion that corresponds with an overall reduction in the piezoelectric response (Figure S8). As such, a change

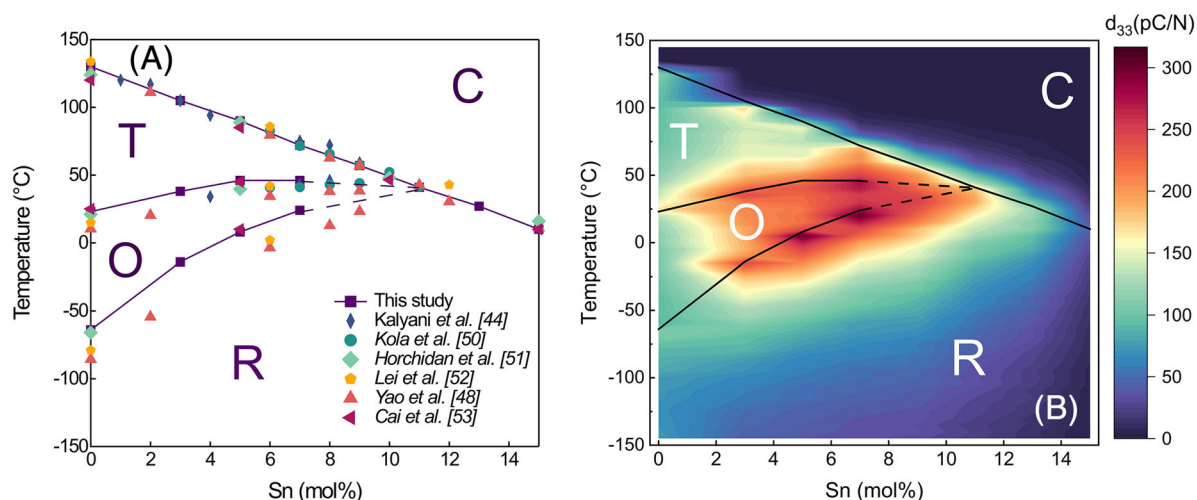


FIGURE 6 Sn-concentration-dependent (A) phase diagram derived from the dielectric data and reported values,^{44,48,50–53} and (B) contour plot of temperature-dependent piezoelectric data at 110 Hz with dielectric phase transitions.

in the domain state, including the domain wall density and mobility, is expected with increasing Sn content.

The T_C is located at higher temperatures than T_d . Near the depolarization temperature, the d_{33} peak at T_C found with Sn content up to 5 mol% is not observed with further increasing Sn content. This peak is due to the rapid increase in permittivity at the phase transition temperature and the loss of electric field-induced macroscopic polarization.^{64,91} The loss of this peak for Sn content above 5 mol% is suggested to be due to the broadening of the dielectric peak at T_C as well as the possible changes in the depolarization behavior due to Sn-induced variations in the domain wall structure. Importantly, this broadness can also be observed in the d_{33} loss at T_d . Interestingly, the piezoelectric response persists at temperatures above the Curie point, clearly indicating that a polarization response remains. Here, the temperature at which $d_{33} < 2$ pC/N is defined as T_{d^*} , where an increase of $\Delta T_C = T_{d^*} - T_C$ and $\Delta T_d = T_{d^*} - T_d$, from around 4°C in BT to 55°C in BTSn15, was observed (Figure S10B). In other words, it was found that a more significant portion of the remaining d_{33} persists above the T_C within the cubic phase with increasing Sn content, suggesting an increase in the broadening and the increased persistence of polar order in the cubic phase, and corresponding well to previous observations in the dielectric response (Figure 4A). Moreover, both the sharpness and the overall value of the piezoelectric maxima decrease and broaden as the Sn-content increases. As previously noted, this also indicates a shift toward a relaxor phase transition with increasing Sn-content. The phenomenon of observing a d_{33} above the T_C is known for more relaxor-like systems, often possessing polar nanoregions (PNRs),^{42,52} which have been observed with high-resolution transmission electron microscopy

(HRTEM) starting from 15 mol% Sn,^{87,92,93} and with high-angle annular dark-field imaging in combination with energy dispersive X-ray mapping and annular bright field imaging in 20 mol% Sn samples.⁹⁴ Another possibility is the occurrence of chemical heterogeneity that leads to the loss of the long-range polar interaction.^{57,94–96} The transition toward a pseudocubic relaxor-like system for Sn-content > 7 mol% Sn at room temperature was already shown in the XRD data (Figure 2). For a higher symmetry structure with lower spontaneous polarization, lower piezoelectric properties can be expected. Moreover, BT exhibits an additional peak in the piezoelectric data around –30°C, which cannot be correlated to the known phase boundaries and is more pronounced at a lower frequency with an unknown origin.

Using the dielectric and piezoelectric data, a phase diagram is shown in Figure 6A, including a comparison with previous reports,^{44,48,50–53} where the anomalies in the small signal responses were used to determine the phase boundaries. The phase diagram is in good agreement with the already reported phase transition temperatures, especially the Curie point shows very good agreement for all the compositions. On the other hand, some reports presented overall lower temperature values for T_{RO} and T_{OT} . These deviations might occur because of differences in processing conditions, leading to a large impact on the small signal properties. Different processing conditions can change grain size,^{73,97,98} porosity, crystallinity, and density, in addition to the measurement techniques themselves, as well as additional surface treatments that can also affect the observed electromechanical properties.^{61,99} Overall, the phase diagram shows a linear decrease of T_C with increasing Sn content, whereas the ferroelectric-ferroelectric R-O and O-T phase transition temperatures

increase until a multi-phase region occurs between 7 and 11 mol% Sn. To predict the approximate phase boundaries within this region, dashed lines are extrapolated in the multiphase region using literature values from Kola et al.⁵⁰ and Yao et al.⁴⁸ In BTSn9, the R-O and O-T boundaries, unlike previous reports, were not observed; small contributions, like underlying peaks, might not be resolved because of the broadening of the signal of relative permittivity with Sn doping. However, an additional underlying peak is visible in the piezoelectric data. The coexistence of phases has been demonstrated by a combination of methods, including XRD, Raman, and HRSTEM imaging.⁴² The origin of this multi-phase or coexistence region is not fully understood yet, but there have been computational investigations suggesting the existence of a quadruple point⁴⁸ or the coexistence of four phases,⁴² leading to increased piezoelectric properties through reduced energy barriers for the expansion and rotation of the polarization.⁴⁷ Kalyani et al.⁴⁴ questioned this theory since the coexistence of four phases for a (pseudo) binary composition is thermodynamically unlikely according to the Gibbs phase rule. Our XRD data, as shown above, support the shift of phase boundaries and suggest the possible coexistence of different phases; however, they do not fully resolve the underlying crystal structures in this region. For reference, comparable multiphase regions were observed before in compositions like BCZT ($\text{Ba}(\text{Ti}_{0.8}\text{Zr}_{0.2})\text{O}_3-(\text{Ba}_{0.7}\text{Ca}_{0.3})\text{TiO}_3$).¹⁰⁰

In order to investigate the role of these phase boundaries on the electromechanical response, a contour plot showing the d_{33} values across these phase boundaries is shown in Figure 6B. Interestingly, the highest piezoelectric properties for BTSn100x are observed at the R-O phase transition. This deviates from previous publications that found maximized electromechanical properties at the O-T phase transition.^{47,48} It is important to note that the method of investigation can strongly alter the observed performance of ferroelectric materials. Not only do material properties such as crystal and microstructure influence maximum piezoelectric values, but measurement parameters, for instance, whether the samples are being measured during cooling or heating, also play a significant role.⁶¹ Measuring across phase transition temperatures can lower these values due to depolarization caused by structural changes, as observed in KNN, where cycling across the O-T boundary resulted in a 20–30% reduction of d_{33} .⁹⁹ Since the starting temperature of this measurement is -150°C , the sample already underwent an R-O phase transition before reaching room temperature during heating. Therefore, maximum properties around the R-O transition might occur due to the decrease in polarization by crossing over different phase transitions before reaching the T_{OT} . This means measuring during heating might lower

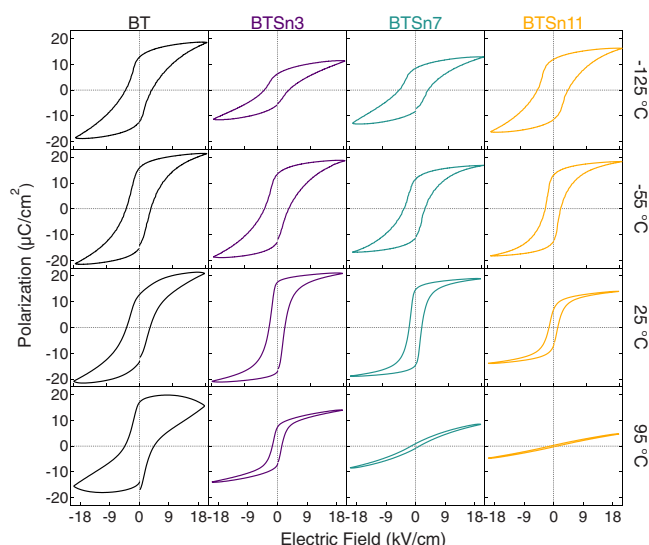


FIGURE 7 Representative polarization–electric field hysteresis of BT, BTSn3, BTSn7, and BTSn11 at 1 Hz and 2 kV/mm.

values around T_{OT} , explaining the deviations from earlier reports that began measuring the sample from room temperature. Interestingly, Liu et al.⁴⁷ also observed that the maximum piezoelectric properties did not occur near the phase coexistence region/point but rather at 9 mol% Sn at 50°C within the T phase and overall heightened values for various concentrations around the O-T boundary. They attributed this deviation to an interplay between the order parameter polarization and the anisotropy energy, specifically, a lowering of the energy barrier for polarization reorientation, while also noting the apparent contradiction that the spontaneous polarization retention is reduced.⁴⁷ As such, the temperature-dependent ferroelectric measurements can further explain the impact Sn-doping has on the phase boundaries of BT, as well as the electromechanical behavior. Furthermore, analyzing the reversible and irreversible contributions to the piezoelectric coefficient can help explain the observed enhancement in electromechanical properties, as discussed below.

3.4 | Temperature-dependent ferroelectric response

The ferroelectric response is examined to gain insight into the influence of Sn on the large field hysteretic behavior, which can modify photoferroelectric properties¹⁰¹ through internal electric fields.^{20,102,103} In addition, temperature-dependent measurements reveal the effect of the aforementioned phase boundaries on the polarization-electric field hysteresis. Figure 7 shows representative polarization-electric field hysteresis curves for BT, BTSn3, BTSn7, and BTSn11 at -125 , -55 , 25 , and 95°C , respectively,

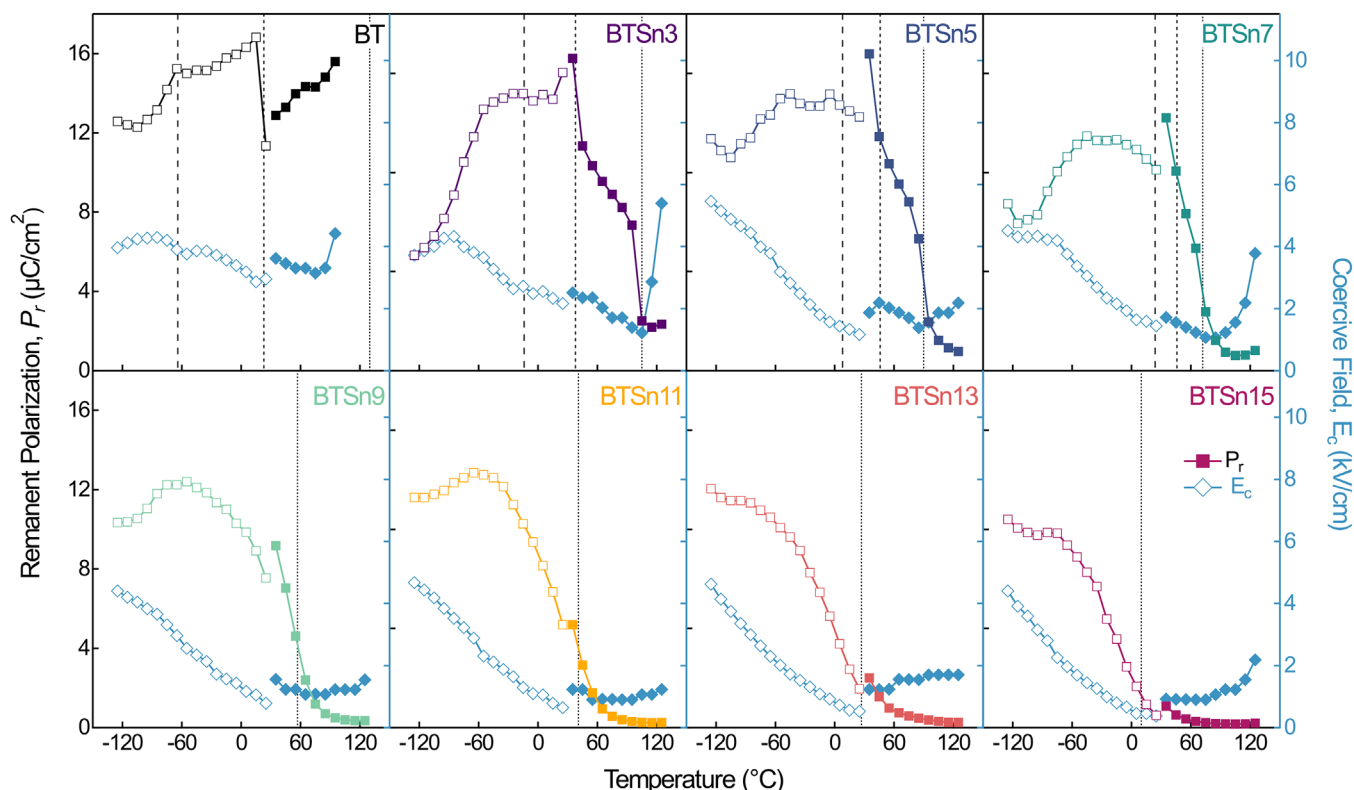


FIGURE 8 Polarization electric field hysteresis analysis with temperature-dependent remanent polarization P_r and coercive field E_c at 1 Hz and 2 kV/mm.

measured at 1 Hz. All samples exhibit ferroelectric behavior except BTSn11 at 95°C, which is in the paraelectric region at this temperature (Figure 7). The shape of the hysteresis curve changes depending on the Sn-content and the measurement temperature. At room temperature, the remanent polarization (P_r) initially rises from BT to BTSn3, followed by a decrease in polarization as Sn content increases. The lower polarization in BT might occur due to the vicinity to the transition temperature at RT, where it is known that the P_r significantly changes at phase boundaries.¹⁰⁴ The reduction in polarization by Sn incorporation might be explained by the smaller grain size of Sn-doped samples, consequently, leading to a higher grain boundary density.^{105,106} At grain boundaries, the permittivity is reduced, and space charges counteract polarizability.⁵³ Further, the inclusion of Sn has been reported to lower the ferroelectric response, further reducing polarization as the Sn content rises.¹⁰⁷ At elevated temperatures, the samples show diminished ferroelectric response due to the proximity to the respective Curie point,⁶¹ and in BT, a stronger increase in conductivity is visible. A tilting of all hysteresis loops is also observed, which diminishes toward RT and is more pronounced at lower and higher temperatures, indicating potential for enhanced energy storage capacity.^{29,61} Additionally, an overall reduction in coercive field (E_c)

with Sn doping is observed. These trends also align well with earlier reports.^{47,50,53,55,56} As such, the hysteresis curve becomes slimmer, resulting in more relaxor-like behavior, consistent with the increased diffuse dielectric response mentioned earlier. Sn-substituted samples with content above 20 mol% Sn were reported to exhibit relaxor behavior.^{78,92,94,108}

To better understand the effect of temperature on Sn-doped BT P_r and E_c are shown for all compositions over the full temperature range in Figure 8. The structural phase transition temperatures, determined from the dielectric data, are marked with dashed lines to highlight the influence of phase boundaries and structural changes with Sn content on the evolution of P_r . Initially, as the temperature increases from -150°C , P_r increases and the E_c decreases due to enhanced domain wall mobility,¹⁰⁹ driven by additional thermal energy.¹¹⁰ In general, a trend of increased P_r is visible when approaching phase boundaries, particularly around polymorphic phase transitions, where an abnormal increase was observed.⁶¹ Subsequently, the actual phase transition temperatures are mostly located at a strong reduction in P_r . Near the ferroelectric-paraelectric phase transition, the P_r decrease also corresponds to a relatively low E_c value. Importantly, with higher Sn content, the P_r decrease becomes more gradual, which is expected for a transition to a more relaxor-like material with PNRs. As

Sn shifts the start of the P_r decrease toward lower temperatures, likely due to the increased rhombohedral phase content and lower E_C , which enhances the reorientation ability. It was reported that the tetragonal phase is harder to switch than the rhombohedral phase for lower coercive fields in the rhombohedral phase at room temperature.¹¹¹ The decrease in E_C with temperature facilitates easier poling, indicating an increased electric field-induced mobility of the domain walls. At even higher temperatures, more thermal fluctuations occur, breaking the long-range order of ferroelectric domains by weakening the interaction between domains and charged defects.⁶¹ Hence, P_r decreases more rapidly, alongside a reduction in E_C and overall maximum polarization, as a result of Sn doping. The increase of P_r and E_C at temperatures beyond the Curie point occurs due to increased conductivity and does not represent a physically significant increase in either value.

For relaxor materials above 20 mol% Sn, previous investigations of the low-temperature ferroelectric response reveal a similar Sn content-dependent shift of the P_r decrease,^{77,112} which has been explained with the random distribution of nanodomains.¹¹³ For the ferroelectric compositions, mainly high-temperature investigations,^{60,114,115} and only a few single low-temperature measurements have been conducted.^{49,116,117} For example, an investigation of 4 mol% Sn as a function of sintering temperature revealed an increase in P_r and a decrease in E_C with larger average grain size.⁴⁹ For 8, 10.5, and 14 mol% Sn, a flattening of the P_r with higher fields was shown.¹¹⁶ For 5 and 11 mol% Sn, a sharp saturation of P_r curve around the phase transitions for low Sn content samples was reported.¹¹⁷ It should be noted that a constant electric field was applied to all compositions in this investigation, which neglects that E_C changes with Sn content, meaning that the different compositions are exposed to varying multiples of their own E_C . Therefore, the observed P_r behavior with increased Sn content might be compared with the electric field-dependent P_r response.¹¹⁶ The importance of this measurement lies in its demonstration that increasing Sn content at lower temperatures provides high polarizability combined with lower E_C , enabling potential applications in new low-temperature areas. Furthermore, the overall ferroelectric response, including polarizability, is influenced by domain wall mobility. Therefore, a Rayleigh-type analysis was conducted to evaluate the impact of Sn on domain wall mobility.

3.5 | Reversible and irreversible piezoelectric contribution

The reversible and irreversible contributions to the piezoelectric response can be obtained with Rayleigh analysis

by measuring d_{33} as a function of stress amplitude.¹⁰⁹ Figure 9 presents the temperature-dependent piezoelectric response with a ± 0.5 to ± 3 MPa stress amplitude over the investigated temperature range. The same phase transitions observed in the frequency-dependent piezoelectric data (black lines) above are also visible here. Moreover, shoulders are observed in the low temperature phases that do not correspond to a known phase transition temperature, and are especially visible for high-stress amplitudes. In BT, it occurs in the O phase, while in all Sn-doped samples, the shoulder was found in the low-temperature R phase. These shoulders could be an inherent material property or might possibly occur due to the influence of vacancies or domain freezing, which could explain why they are particularly visible at high stress amplitudes. Furthermore, the starting temperature of stress amplitude dispersion shifts to higher temperatures with increasing Sn content. For BT, full dispersion is already visible at -150°C , whereas for the Sn-doped samples, it occurs at higher temperatures. This is unexpected given the lower E_C in Sn-doped samples, where one would expect higher domain wall mobility. However, as the material is more susceptible to external forces, the prestress might mechanically clamp domains and thereby decrease domain wall mobility. Additionally, for BTsn9-15, the dispersion extends beyond the peak of the paraelectric-ferroelectric transition. In contrast, a sharp drop and the end of the dispersion are observed at the transition maximum for BT-BTsn7. A reason for this relaxation into the paraelectric phase might be the appearance of PNRs, as previously explained.

As a general trend, higher d_{33} values can be expected with increasing stress amplitude, assuming the measurement conditions remain below the coercive stress threshold where ferroelastic domain switching mechanically depolarizes the material.⁶⁴ This behavior is observed for all compositions in the ferroelectric phase. Notably, BT-BTsn7 displays a reversed trend after the maximum of the paraelectric-ferroelectric transition, which is a measurement artifact resulting from the sharp decrease in polarization in this temperature region. In BT, the temperature difference between the T_C and T_{d^*} occurs over a relatively small temperature region $\Delta T_C = 2^\circ\text{C}$, compared with higher Sn content samples that show a broader temperature region. For example, BTsn15 exhibits a $\Delta T_C = 55^\circ\text{C}$. This also corresponds with the above-mentioned possible change toward a relaxor phase transition with increasing Sn-content. The highest d_{33} values at room temperature are again observed for BTsn7, which is related to the proximity of the phase transition boundaries.

To better understand the domain wall mobility and the contributions to the piezoelectric coefficient, the Rayleigh coefficients were determined (Figure 10). This approach allows for the estimation of both reversible and irreversible

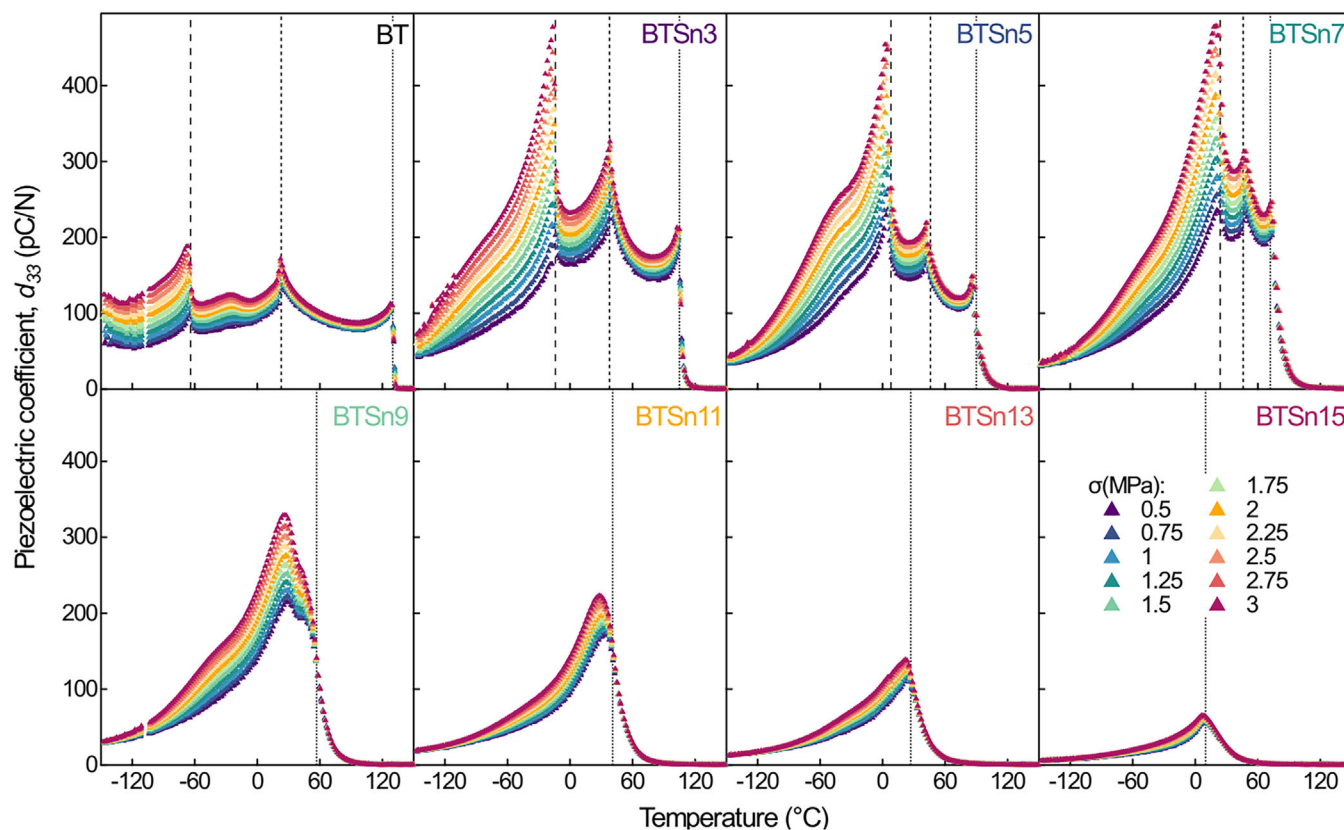


FIGURE 9 Stress amplitude-dependent piezoelectric coefficient between 0.5 and 3 MPa. Black dashed lines indicate phase transition temperatures estimated from temperature-dependent dielectric anomaly.

contributions to the piezoelectric charge coefficient.¹⁰⁹ Since the applied stress amplitudes (± 0.5 to ± 3 MPa) were well below the coercive stress, which was found to be approximately -25 MPa in polycrystalline BT,¹¹⁸ the linear equation for the stress amplitude-dependent piezoelectric charge coefficient can be applied: $d_{33}(\sigma_0) = d_{\text{init}} + \alpha\sigma_0$, where d_{init} is the Rayleigh parameter for the reversible contribution, α accounts for the irreversible contributions, and σ_0 denotes the applied stress amplitude. The irreversible contributions arise from polarization changes, such as ferroelectric switching or irreversible domain wall motion, amongst others. Irreversible domain wall motion may be induced by the pinning of domain walls under external mechanical or electrical driving forces.^{71,109} The parameter α , representing the rate of change of $d_{33}(\sigma_0)$, is determined from the slope of the linear equation for each temperature set, as shown in Figure 10A. All phase boundaries are apparent across all compositions, and the previously described shoulder is also observed. As observed above, the highest irreversible contributions coincide with the R–O or R–C phase boundaries, corresponding well to piezoelectric measurements (Figure 6). This correlation arises because α increases with larger stress amplitude dispersions, which is especially visible at these phase transitions (Figure 9). Notably, the highest irreversible contributions

around the R–O boundary are observed for BTSn3, while the highest RT value is again displayed for BTSn7. This means that the maximum piezoelectric coefficient at RT for BTSn7 arises due to dopant-induced enhanced domain wall mobility, where the location of the phase boundaries is critical. Other material systems, such as PZT, also show the highest irreversible extrinsic contributions in the rhombohedral phase compared with other phases.¹⁰⁹ The increase in irreversible extrinsic contributions in the rhombohedral phase may also account for the observed increase in P_R .

Overall, α decreases with increasing Sn content and therefore improves the thermal stability of the material. Previous studies on BT have shown that decreasing grain size leads to a reduction in α due to increased internal stress caused by domain wall clamping.¹⁰⁹ Increased domain wall clamping could occur due to the diminished average grain size, explaining the trend of α . However, an increase in α with smaller grain sizes has also been reported, although in the according study the grain sizes ranged from 0.5 to 5 μm and α was calculated from ferroelectric hysteresis rather than from the direct piezoelectric coefficient.^{119,120} Importantly, the temperature-dependence is critical to consider as phase transition regions have a significant influence on the domain wall

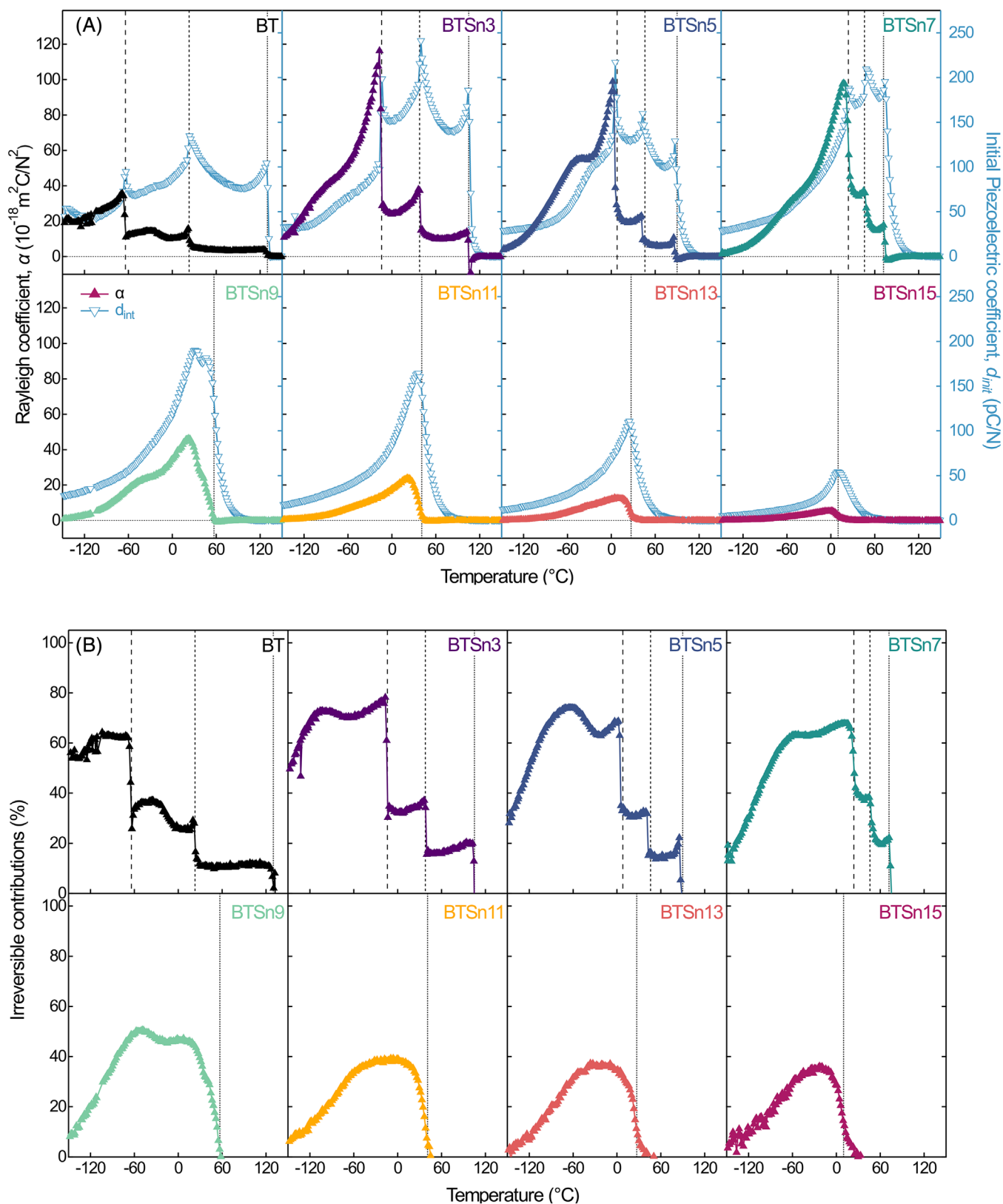


FIGURE 10 Temperature-dependent Rayleigh analysis of (A) irreversible contributions α (colored graphs) and reversible contributions d_{init} (blue graphs) to the piezoelectric charge coefficient, and (B) percentage of irreversible contributions with phase transition temperatures (black lines).

motion and measurements at RT alone may not sufficiently capture the grain size dependency of α due to the important role of proximity to phase boundaries (Figure 1). Apart from that, it should be mentioned that factors such as domain wall mobility as well as defects and space charges, impact the observed macroscopic properties (dielectric, ferroelectric, piezoelectric, etc.) of the material system.^{119,121}

Effects such as reversible domain wall motion or lattice deformation, including unit cell volume changes, belong to the reversible contributions d_{init} (Figure 10A, blue markers), which is the piezoelectric response at zero amplitude.^{71,109} Similarly to α , all phase transitions are again visible in d_{init} , although the highest values are in the O and T phases for BT-BTSn7. For BTSn9-15, d_{init} is also already the largest in the R phase, with the onset of its growth shifting to higher temperatures as Sn content rises. The highest d_{init} is again observed for BTSn3 (around 241 pC/N) and at RT for BTSn7 (around 176 pC/N), due to phase coexistence. In general, by increasing the Sn content, the reversible contributions become increasingly dominant, and an overall decrease of irreversible and reversible contributions is observed. For one, Sn doping leads to a more symmetric crystal structure with less distortion of the B-site cation, which decreases the lattice strain effect.^{25,122,123} The same trend can be observed with increasing temperature, where the unit cell becomes less distorted at higher temperatures, leading to a decrease in the reversible contributions.

The percentage of irreversible contributions (Figure 10B) to the stress amplitude-dependent piezoelectric charge coefficient combines the above-mentioned observations of α and d_{init} . The dielectric phase transition temperatures (black lines) are again in good agreement with the observed transitions between the different phases. For BT-BTSn7, the highest percentage of irreversible contributions occurs in the R phase. BT shows the start of the growth of irreversible contributions even below -150°C , with this onset shifting to higher temperatures as the Sn content increases. BTSn3 exhibits the highest value around the R-O phase boundary. As Sn content increases, the percentage of irreversible contributions decreases and the sharp depolarization transition broadens. Interestingly, for high Sn content samples, such as BTSn15, irreversible contributions appear to persist above the Curie point, corresponding well with the observed d_{33} response above T_c (Figures 4B and 9). The above-mentioned underlying peak is particularly visible in the percentage of irreversible contributions. The enhanced irreversible contributions in the rhombohedral phase are in good agreement with the high P_r values shown in the same phase.⁶¹ However, further local and macro-scale investigations on domain

structure dynamics and the correlation to the electrochemical behavior are needed to better understand the origin of these phenomena.

4 | CONCLUSION


This comprehensive study investigated the temperature-dependent electromechanical properties, including structural, dielectric, ferroelectric, and piezoelectric characteristics, of photoferroelectric $\text{BaSn}_x\text{Ti}_{1-x}\text{O}_3$ ($x = 0, 0.03, 0.05, 0.07, 0.09, 0.11, 0.13$, and 0.15). The crystal structure of BaTiO_3 was significantly altered with increasing Sn content, transitioning from a R distortion at approximately -100°C , through O and T phases, toward a C structure above T_c . Correspondingly, the phase transitions between lower symmetry ferroelectric phases shifted to higher temperatures with increasing Sn content, while T_c decreased, eventually leading to a multiphase region, which is in good agreement with previous studies. Maximized piezoelectric values were determined with measurements of the temperature-dependent electromechanical response, occurring especially near the R-O phase boundary, for example, around 400 pC/N for 7 mol% Sn, but also around O-T phase transitions, differing from previous reports. The polarization response from -125°C to 125°C shows an initial P_r increase, followed by a gradual decrease with higher Sn content and a relatively low E_C , likely due to increased domain wall mobility. Insights into the reversible and irreversible contributions to the piezoelectric charge coefficient were examined between -150°C and 150°C , highlighting their impact and the necessity of balancing these to achieve an enhanced electromechanical response through Sn incorporation. The observed increase in the diffusiveness of the phase boundaries, the persistence of the piezoelectric response into the cubic phase, and the slimming of the ferroelectric hysteresis loops further support the trend toward a relaxor-like state induced by Sn doping. However, further research is required to fully understand the observed polarization behavior and piezoelectric response, particularly through studies of domain wall dynamics, to be able to design more efficient photoferroelectric materials.

ACKNOWLEDGMENTS

VK, UE, MK, and KGW gratefully acknowledge the financial support for this work from the Deutsche Forschungsgemeinschaft under grant no. GRK2495/F/H/S. BGM thanks the Australian Institute for Nuclear Science and Engineering for a PGRA scholarship.

Open access funding enabled and organized by Projekt DEAL.

ORCID

Viktoria Kraft  <https://orcid.org/0009-0002-7239-518X>
 Udo R Eckstein  <https://orcid.org/0000-0001-9546-8463>
 Michel Kuhfuß  <https://orcid.org/0009-0002-2533-3509>
 Neamul H Khansur  <https://orcid.org/0000-0001-8769-3329>
 Frederick P Marlton  <https://orcid.org/0000-0001-9071-7109>
 Bryce Mullens  <https://orcid.org/0000-0002-1953-1077>
 Alexander Martin  <https://orcid.org/0000-0002-6218-8390>
 Koichi Hayashi  <https://orcid.org/0000-0002-8782-4293>
 Kyle G Webber  <https://orcid.org/0000-0002-1283-7874>

REFERENCES

- Green MA. Photovoltaic principles. *Physica E*. 2002;14:11–17. [https://doi.org/10.1016/S1386-9477\(02\)00354-5](https://doi.org/10.1016/S1386-9477(02)00354-5)
- Zhu S, Wang D. Photocatalysis: basic principles, diverse forms of implementations and emerging scientific opportunities. *Adv Energy Mater*. 2017;7:1700841. <https://doi.org/10.1002/aenm.201700841>
- Bai Y, Jantunen H, Juuti J. Ferroelectric oxides for solar energy conversion, multi-source energy harvesting/sensing, and opto-ferroelectric applications. *ChemSusChem*. 2019;12:2540–49. <https://doi.org/10.1002/cssc.201900671>
- Yudin PV, Tagantsev AK. Fundamentals of flexoelectricity in solids. *Nanotechnology*. 2013;24:432001. <https://doi.org/10.1088/0957-4484/24/43/432001>
- Jaffe B, Cook WR, Jaffe HL. Piezoelectric ceramics. London, New York: Academic Press; 1971.
- Zhang D, Wu H, Bowen CR, Yang Y. Recent advances in pyroelectric materials and applications. *Small*. 2021;17:2103960. <https://doi.org/10.1002/smll.202103960>
- Fiebig M. Revival of the magnetoelectric effect. *J Phys D: Appl Phys*. 2005;38:R123–52. <https://doi.org/10.1088/0022-3727/38/8/R01>
- Abbas Q, Mirzaei M, Hunt MRC, Hall P, Raza R. Current state and future prospects for electrochemical energy storage and conversion systems. *Energies*. 2020;13:5847. <https://doi.org/10.3390/en13215847>
- Bai Y, Jantunen H, Juuti J. Energy harvesting research: the road from single source to multisource. *Adv Mater*. 2018;30:1707271. <https://doi.org/10.1002/adma.201707271>
- Hao J, Xu C-N. Piezophotonics: from fundamentals and materials to applications. *MRS Bull*. 2018;43:965–69. <https://doi.org/10.1557/mrs.2018.296>
- Kundys B, Viret M, Colson D, Kundys DO. Light-induced size changes in BiFeO₃ crystals. *Nat Mater*. 2010;9:803–5. <https://doi.org/10.1038/nmat2807>
- Fiebig M, Lottermoser T, Meier D, Trassin M. The evolution of multiferroics. *Nat Rev Mater*. 2016;1:1–14. <https://doi.org/10.1038/natrevmats.2016.46>
- Grinberg I, West DV, Torres M, Gou G, Stein DM, Wu L, et al. Perovskite oxides for visible-light-absorbing ferroelectric and photovoltaic materials. *Nature*. 2013;503:509–12. <https://doi.org/10.1038/nature12622>
- Bai Y, Tofel P, Palosaari J, Jantunen H, Juuti J. A game changer: a multifunctional perovskite exhibiting giant ferroelectricity and narrow bandgap with potential application in a truly monolithic multienergy harvester or sensor. *Adv Mater*. 2017;29:1700767. <https://doi.org/10.1002/adma.201700767>
- Bai Y, Xiang H, Jantunen H, Juuti J. Multi-functional perovskites – an investigation of compositional and processing influence on microstructure, dielectric and ferroelectric properties. *Eur Phys J: Spec Top*. 2019;228:1555–73. <https://doi.org/10.1140/epjst/e2019-800132-8>
- Bai Y, Palosaari J, Tofel P, Juuti J. A single-material multi-source energy harvester, multifunctional sensor, and integrated harvester-sensor system—demonstration of concept. *Energy Technol*. 2020;8:2000461. <https://doi.org/10.1002/ente.202000461>
- Catalan G, Scott JF. Physics and Applications of Bismuth Ferrite. *Adv Mater*. 2009;21:2463–85. <https://doi.org/10.1002/adma.200802849>
- Némec P, Fiebig M, Kampfrath T, Kimel AV. Antiferromagnetic opto-spintronics. *Nat Phys*. 2018;14:229–41. <https://doi.org/10.1038/s41567-018-0051-x>
- Butler KT, Frost JM, Walsh A. Ferroelectric materials for solar energy conversion: photoferroics revisited. *Energy Environ Sci*. 2015;8:838–48. <https://doi.org/10.1039/C4EE03523B>
- Paillard C, Bai X, Infante IC, Guennou M, Geneste G, Alexe M, et al. Photovoltaics with ferroelectrics: current status and beyond. *Adv Mater*. 2016;28:5153–68. <https://doi.org/10.1002/adma.201505215>
- Hua H, Bao G, Li C, Zhu Y, Yang J, Li X. Effect of Ho, Mn co-doping on the structural, optical and ferroelectric properties of BiFeO₃ nanoparticles. *J Mater Sci: Mater Electron*. 2017;28:17283–87. <https://doi.org/10.1007/s10854-017-7660-5>
- Koch WTH, Munser R, Ruppel W, Würfel P. Bulk photovoltaic effect in BaTiO₃. *Solid State Commun*. 1975;17:847–50. [https://doi.org/10.1016/0038-1098\(75\)90735-8](https://doi.org/10.1016/0038-1098(75)90735-8)
- Acosta M, Novak N, Rojas V, Patel S, Vaish R, Koruza J, et al. BaTiO₃-based piezoelectrics: fundamentals, current status, and perspectives. *Appl Phys Rev*. 2017;4:041305. <https://doi.org/10.1063/1.4990046>
- Kreisel J, Alexe M, Thomas PA. A photoferroelectric material is more than the sum of its parts. *Nat Mater*. 2012;11:260–260. <https://doi.org/10.1038/nmat3282>
- Huan Y, Wang X, Li L, Koruza J. Strong domain configuration dependence of the nonlinear dielectric response in (K,Na)NbO₃-based ceramics. *Appl Phys Lett*. 2015;107:202903. <https://doi.org/10.1063/1.4936165>
- Abebe M, Brajesh K, Malhotra JS, Ranjan R. Rayleigh analysis of domain dynamics across temperature induced polymorphic phase transitions in lead-free piezoceramics (1-x)(BaTi_{0.88}Sn_{0.12})-x(Ba_{0.7}Ca_{0.3})TiO₃. *J Phys D: Appl Phys*. 2018;51:185601. <https://doi.org/10.1088/1361-6463/aaab75e>
- Kola L, Murali D, Pal S, Nanda BRK, Murugavel P. Enhanced bulk photovoltaic response in Sn doped BaTiO₃ through composition dependent structural transformation. *Appl Phys Lett*. 2019;114:183901. <https://doi.org/10.1063/1.5088635>
- Pal S, Muthukrishnan S, Sadhukhan B, S NV, Murali D, Murugavel P. Bulk photovoltaic effect in BaTiO₃-based

- ferroelectric oxides: an experimental and theoretical study. *J Appl Phys*. 2021;129:084106. <https://doi.org/10.1063/5.0036488>
29. Veerapandiyan V, Benes F, Gindel T, Deluca M. Strategies to improve the energy storage properties of perovskite lead-free relaxor ferroelectrics: a review. *Materials*. 2020;13:5742. <https://doi.org/10.3390/ma13245742>
 30. Zhao C, Huang Y, Wu J. Multifunctional barium titanate ceramics via chemical modification tuning phase structure. *InfoMat*. 2020;2:1163–90. <https://doi.org/10.1002/inf2.12147>
 31. Yoon S-H, Randall CA, Hur K-H. Influence of grain size on impedance spectra and resistance degradation behavior in acceptor (Mg)-doped BaTiO₃ ceramics. *J Am Ceram Soc*. 2009;92:2944–52. <https://doi.org/10.1111/j.1551-2916.2009.03305.x>
 32. Buscaglia V, Buscaglia MT, Canu G. BaTiO₃-based ceramics: fundamentals, properties and applications. *Encyclopedia of materials: technical ceramics and glasses*. Elsevier; 2021. p. 311–44. <https://doi.org/10.1016/B978-0-12-803581-8.12132-0>
 33. Rahman MA, Hasan Z, Islam J, Das DK, Chowdhury FI, Khandaker MU, et al. Tailoring the properties of bulk BaTiO₃ based perovskites by heteroatom-doping towards multifunctional applications: a review. *ECS J Solid State Sci Technol*. 2023;12:103015. <https://doi.org/10.1149/2162-8777/ad00da>
 34. Rahman MA. Understanding of doping sites and versatile applications of heteroatom modified BaTiO₃ ceramic. *J Asian Ceram Soc*. 2023;11:215–24. <https://doi.org/10.1080/21870764.2023.2203635>
 35. Xue D, Zhou Y, Bao H, Zhou C, Gao J, Ren X. Elastic, piezoelectric, and dielectric properties of Ba(Zr_{0.2}Ti_{0.8})O₃₋₅₀(Ba_{0.7}Ca_{0.3})TiO₃ Pb-free ceramic at the morphotropic phase boundary. *J Appl Phys*. 2011;109:054110. <https://doi.org/10.1063/1.3549173>
 36. Panda PK, Sahoo B, Thejas TS, Krishna M. High d_{33} lead-free piezoceramics: a review. *J Electron Mater*. 2022;51:938–52. <https://doi.org/10.1007/s11664-021-09346-0>
 37. Li Z, Yu J, Hao S, Janolin P-E. Enhancing properties of lead-free ferroelectric BaTiO₃ through doping. *J Eur Ceram Soc*. 2022;42:4693–701. <https://doi.org/10.1016/j.jeurceramsoc.2022.05.023>
 38. Ali AI, Ahn CW, Kim YS. Enhancement of piezoelectric and ferroelectric properties of BaTiO₃ ceramics by aluminum doping. *Ceram Int*. 2013;39:6623–29. <https://doi.org/10.1016/j.ceramint.2013.01.099>
 39. Infante IC, Volkova H, Gemeiner P, Geneste G, Guillot J, Frontera C, et al. Optical and electronic properties in ferroelectric barium titanate-based compounds. 2019. <https://doi.org/10.17185/duerpublico/4648>
 40. Tihiti M, Ibrahim JEFM, Basyooni MA, Kurovics E, Belaid W, Hussainova I, et al. Role of A-site (Sr), B-site (Y), and A, B sites (Sr, Y) substitution in lead-free BaTiO₃ ceramic compounds: structural, optical, microstructure, mechanical, and thermal conductivity properties. *Ceram Int*. 2023;49:1947–59. <https://doi.org/10.1016/j.ceramint.2022.09.160>
 41. Gatasheh MK, Daoud MS, Kassim H. Bandgap narrowing of BaTiO₃-based ferroelectric oxides through cobalt doping for photovoltaic applications. *Materials*. 2023;16:7528. <https://doi.org/10.3390/ma16247528>
 42. Wang D, Fan Z, Rao G, Wang G, Liu Y, Yuan C, et al. Ultra-high piezoelectricity in lead-free piezoceramics by synergistic design. *Nano Energy*. 2020;76:104944. <https://doi.org/10.1016/j.nanoen.2020.104944>
 43. Liu C-L, Du Q, Wu J-M, Zhang G, Shi Y-S. High piezoelectricity of 3D printed BaTiO_{3-x}BaSnO₃ piezoceramics via vat photopolymerization. *J Eur Ceram Soc*. 2024;44:4639–45. <https://doi.org/10.1016/j.jeurceramsoc.2024.01.085>
 44. Kalyani AK, Brajesh K, Senyshyn A, Ranjan R. Orthorhombic-tetragonal phase coexistence and enhanced piezo-response at room temperature in Zr, Sn, and Hf modified BaTiO₃. *Appl Phys Lett*. 2014;104:252906. <https://doi.org/10.1063/1.4885516>
 45. Singh KC, Nath AK, Laishram R, Thakur OP. Structural, electrical and piezoelectric properties of nanocrystalline tin-substituted barium titanate ceramics. *J Alloys Compd*. 2011;509:2597–601. <https://doi.org/10.1016/j.jallcom.2010.11.106>
 46. Bijalwan V, Kaštyl J, Erhart J, Prajzler V, Tofel P, Sobola D, et al. Optical and electrical performance of translucent BaTiO₃-BaSnO₃ ceramics. *Ceram Int*. 2024;50:28123–32. <https://doi.org/10.1016/j.ceramint.2024.05.111>
 47. Liu W, Wang J, Ke X, Li S. Large piezoelectric performance of Sn doped BaTiO₃ ceramics deviating from quadruple point. *J Alloys Compd*. 2017;712:1–6. <https://doi.org/10.1016/j.jallcom.2017.04.013>
 48. Yao Y, Zhou C, Lv D, Wang D, Wu H, Yang Y, et al. Large piezoelectricity and dielectric permittivity in BaTiO_{3-x}BaSnO₃ system: the role of phase coexisting. *Europhys Lett*. 2012;98:27008. <https://doi.org/10.1209/0295-5075/98/27008>
 49. Tan Y, Viola G, Koval V, Yu C, Mahajan A, Zhang J, et al. On the origin of grain size effects in Ba(Ti_{0.96}Sn_{0.04})O₃ perovskite ceramics. *J Eur Ceram Soc*. 2019;39:2064–75. <https://doi.org/10.1016/j.jeurceramsoc.2019.01.041>
 50. Kola L, Swain AB, Rath M, Rao MSR, Murugavel P. Impedance characteristics and PTCR effect in lead free BaTi_{1-x}Sn_xO₃ piezoceramics. *Mater Res Bull*. 2018;106:371–78. <https://doi.org/10.1016/j.materresbull.2018.06.021>
 51. Horchidan N, Ianculescu AC, Curecheriu LP, Tudorache F, Musteata V, Stoleriu S, et al. Preparation and characterization of barium titanate stannate solid solutions. *J Alloys Compd*. 2011;509:4731–37. <https://doi.org/10.1016/j.jallcom.2011.01.123>
 52. Lei C, Bokov AA, Ye Z-G. Ferroelectric to relaxor crossover and dielectric phase diagram in the BaTiO₃-BaSnO₃ system. *J Appl Phys*. 2007;101:084105. <https://doi.org/10.1063/1.2715522>
 53. Cai W, Fan Y, Gao J, Fu C, Deng X. Microstructure, dielectric properties and diffuse phase transition of barium stannate titanate ceramics. *J Mater Sci: Mater Electron*. 2011;22:265–72. <https://doi.org/10.1007/s10854-010-0126-7>
 54. Kathait GS, Maini S. Dielectric and Piezoelectric Characteristics of Ba(Ti_{1-x}Sn_x)O₃ (BT-xBS) electro-ceramics doped with Sn for 0.07 ≤ x ≤ 0.11. *J Electron Mater*. 2025. <https://doi.org/10.1007/s11664-025-11806-w>
 55. Zhang H, Giddens H, Saunders TG, Palma M, Abrahams I, Yan H, et al. Microwave tunability in tin substituted barium titanate. *J Eur Ceram Soc*. 2024;44:1627–35. <https://doi.org/10.1016/j.jeurceramsoc.2023.10.033>
 56. Horchidan N, Ianculescu AC, Vasilescu CA, Deluca M, Musteata V, Ursic H, et al. Multiscale study of ferroelectric-relaxor crossover in BaSn_xTi_{1-x}O₃ ceramics. *J Eur Ceram Soc*. 2014;34:3661–74. <https://doi.org/10.1016/j.jeurceramsoc.2014.06.005>

57. Deluca M, Stoleriu L, Curecheriu LP, Horchidan N, Ianculescu AC, Galassi C, et al. High-field dielectric properties and Raman spectroscopic investigation of the ferroelectric-to-relaxor crossover in $\text{BaSn}_x\text{Ti}_{1-x}\text{O}_3$ ceramics. *J Appl Phys*. 2012;111:084102. <https://doi.org/10.1063/1.3703672>
58. Ansaree MdJ, Kumar U, Upadhyay S. Solid-state synthesis of nano-sized $\text{Ba}(\text{Ti}_{1-x}\text{Sn}_x)\text{O}_3$ powders and dielectric properties of corresponding ceramics. *Appl Phys A*. 2017;123:432. <https://doi.org/10.1007/s00339-017-1047-6>
59. Marković S, Mitrić M, Jovalekić Č, Miljković M. Dielectric and ferroelectric properties of $\text{BaTi}_{1-x}\text{Sn}_x\text{O}_3$ multilayered ceramics. *Mater Sci Forum*. 2007;555:249–54. <https://doi.org/10.4028/www.scientific.net/MSF.555.249>
60. Upadhyay SK, Reddy VR, Bag P, Rawat R, Gupta SM, Gupta A. Electro-caloric effect in lead-free Sn doped BaTiO_3 ceramics at room temperature and low applied fields. *Appl Phys Lett*. 2014;105:112907. <https://doi.org/10.1063/1.4896044>
61. Jin L, Li F, Zhang S. Decoding the fingerprint of ferroelectric loops: comprehension of the material properties and structures. *J Am Ceram Soc*. 2014;97:1–27. <https://doi.org/10.1111/jace.12773>
62. Wallwork KS, Kennedy BJ, Wang D. The high resolution powder diffraction beamline for the Australian synchrotron. In AIP conference proceedings. vol. 879. Daegu (Korea): AIP; 2007, p. 879–82. <https://doi.org/10.1063/1.2436201>
63. Webber KG, Aulbach E, Key T, Marsilius M, Granzow T, Rödel J. Temperature-dependent ferroelastic switching of soft lead zirconate titanate. *Acta Mater*. 2009;57:4614–23. <https://doi.org/10.1016/j.actamat.2009.06.037>
64. Schader FH, Isaia D, Weber M, Aulbach E, Webber KG. High-temperature stress-dependent piezoelectric and dielectric coefficient of soft $\text{Pb}(\text{Zr,Ti})\text{O}_3$. *J Mater Sci*. 2018;53:3296–308. <https://doi.org/10.1007/s10853-017-1817-8>
65. Sattar H, Bakhtiar SH, Zhou J, Zafar S, Imran M, Abukhadra MR, et al. Simultaneous quantitative analysis of structural and mechanical properties in Sn-doped BaTiO_3 ceramics using a multimodal laser opto-ultrasonic dual detection (LOUD) approach. *Talanta*. 2025;292:127914. <https://doi.org/10.1016/j.talanta.2025.127914>
66. Marković S, Jovalekić Č, Veselinović L, Mentus S, Uskoković D. Electrical properties of barium titanate stannate functionally graded materials. *J Eur Ceram Soc*. 2010;30:1427–35. <https://doi.org/10.1016/j.jeurceramsoc.2009.10.020>
67. Jiang Z, Huang J, Yuan R, Xu N, Jiang Y, Zhang J, et al. Phase evolution and local piezoelectric response of Sn-Doped BaTiO_3 ceramics. *Physica Status Solidi (a)*. 2022;219:2200344. <https://doi.org/10.1002/pssa.202200344>
68. Du F, Cui B, Cheng H, Niu R, Chang Z. Synthesis, characterization, and dielectric properties of $\text{Ba}(\text{Ti}_{1-x}\text{Sn}_x)\text{O}_3$ nanopowders and ceramics. *Mater Res Bull*. 2009;44:1930–34. <https://doi.org/10.1016/j.materresbull.2009.05.001>
69. Shihua D, Tianxiu S, Xiaojing Y, Guanghua L. Effect of grain size of BaTiO_3 ceramics on dielectric properties. *Ferroelectrics*. 2010;402:55–59. <https://doi.org/10.1080/00150191003697377>
70. Kong LB, Huang H, Li S. Fundamentals of ferroelectric materials. In: Huang H, Scott JF, editors. *Ferroelectric materials for energy applications*. 1st ed. Wiley; 2018, p. 1–31. <https://doi.org/10.1002/9783527807505.ch1>
71. Damjanovic D. Stress and frequency dependence of the direct piezoelectric effect in ferroelectric ceramics. *J Appl Phys*. 1997;82:1788–97. <https://doi.org/10.1063/1.365981>
72. Xu Y, Shao G, Zhou Y, Wang Y, Yang S, Ding X, et al. History dependence of avalanche dynamics of ferroelectric phase transition in BaTiO_3 under external bias field. *Appl Phys Lett*. 2023;122:022903. <https://doi.org/10.1063/5.0133020>
73. Arlt G, Hennings D, De With G. Dielectric properties of fine-grained barium titanate ceramics. *J Appl Phys*. 1985;58:1619–25. <https://doi.org/10.1063/1.336051>
74. Ghosh D, Sakata A, Carter J, Thomas PA, Han H, Nino JC, et al. Domain wall displacement is the origin of superior permittivity and piezoelectricity in BaTiO_3 at intermediate grain sizes. *Adv Funct Mater*. 2014;24:885–96. <https://doi.org/10.1002/adfm.201301913>
75. Jona F, Shirane G, Shirane G. *Ferroelectric crystals*. Republ. New York, NY: Dover Publ; 1993.
76. Leist T, Webber KG, Jo W, Aulbach E, Rödel J, Prewitt AD, et al. Stress-induced structural changes in La-doped BiFeO_3 – PbTiO_3 high-temperature piezoceramics. *Acta Mater*. 2010;58:5962–71. <https://doi.org/10.1016/j.actamat.2010.07.012>
77. Wei X, Yao X. Preparation, structure and dielectric property of barium stannate titanate ceramics. *Mater Sci Eng B*. 2007;137:184–88. <https://doi.org/10.1016/j.mseb.2006.11.012>
78. Kleemann W. Random fields in relaxor ferroelectrics — a jubilee review. *J Adv Dielectric*. 2012;02:1241001. <https://doi.org/10.1142/S2010135X12410019>
79. Canu G, Confalonieri G, Deluca M, Curecheriu L, Buscaglia MT, Asandulesa M, et al. Structure-property correlations and origin of relaxor behaviour in $\text{BaCe}_x\text{Ti}_{1-x}\text{O}_3$. *Acta Mater*. 2018;152:258–68. <https://doi.org/10.1016/j.actamat.2018.04.038>
80. Akishige Y, Nakanishi T, Mōri N. Dielectric dispersion in BaTiO_3 single crystal at low temperatures. *Ferroelectrics*. 1998;217:217–22. <https://doi.org/10.1080/00150199808015041>
81. Ochoa DA, Esteves G, Jones JL, Rubio-Marcos F, Fernández JF, García JE. Extrinsic response enhancement at the polymorphic phase boundary in piezoelectric materials. *Appl Phys Lett*. 2016;108:142901. <https://doi.org/10.1063/1.4945593>
82. Shi C, Han X-B, Zhang W. Structural phase transition-associated dielectric transition and ferroelectricity in coordination compounds. *Coord Chem Rev*. 2019;378:561–76. <https://doi.org/10.1016/j.ccr.2017.09.020>
83. Fujimoto M. *The physics of structural phase transitions*. 2nd ed. New York: Springer; 2005.
84. Damjanovic D. Ferroelectric, dielectric and piezoelectric properties of ferroelectric thin films and ceramics. *Rep Prog Phys*. 1998;61:1267–324. <https://doi.org/10.1088/0034-4885/61/9/002>
85. Shvartsman VV, Dec J, Xu ZK, Banyas J, Keburis P, Kleemann W. Crossover from ferroelectric to relaxor behavior in $\text{BaTi}_{1-x}\text{Sn}_x\text{O}_3$ solid solutions. *Phase Transitions*. 2008;81:1013–21. <https://doi.org/10.1080/01411590802457888>
86. Mueller V, Kouvatov A, Steinhäuser R, Beige H, Abicht H-P. Ferroelectric and relaxor-like electromechanical strain in $\text{BaTi}_{1-x}\text{Sn}_x\text{O}_3$ ceramics. *Integr Ferroelectr*. 2004;63:81–84. <https://doi.org/10.1080/10584580490458694>
87. Ren P, Liu Z, Wang Q, Peng B, Ke S, Fan H, et al. Large non-linear dielectric behavior in $\text{BaTi}_{1-x}\text{Sn}_x\text{O}_3$. *Sci Rep*. 2017;7:6693. <https://doi.org/10.1038/s41598-017-07192-x>

88. Baskaran N, Chang H. Effect of Sn doping on the phase transformation properties of ferroelectric BaTiO₃. *J Mater Sci: Mater Electron*. 2001;12:527–31. <https://doi.org/10.1023/A:1012453526652>
89. Schader FH, Morozov M, Wefring ET, Grande T, Webber KG. Mechanical stability of piezoelectric properties in ferroelectric perovskites. *J Appl Phys*. 2015;117:194101. <https://doi.org/10.1063/1.4919815>
90. Seshadri SB, Prewitt AD, Studer AJ, Damjanovic D, Jones JL. An in situ diffraction study of domain wall motion contributions to the frequency dispersion of the piezoelectric coefficient in lead zirconate titanate. *Appl Phys Lett*. 2013;102:042911. <https://doi.org/10.1063/1.4789903>
91. Sundar V, Newnham RE. Electrostriction and polarization. *Ferroelectrics*. 1992;135:431–46. <https://doi.org/10.1080/00150199208230043>
92. Xie L, Li YL, Yu R, Cheng ZY, Wei XY, Yao X, et al. Static and dynamic polar nanoregions in relaxor ferroelectric Ba(Ti_{1-x}Sn_x)O₃ system at high temperature. *Phys Rev B*. 2012;85:014118. <https://doi.org/10.1103/PhysRevB.85.014118>
93. Volkova H. Photo-response of ferroelectric oxides. Ph.D.thesis. Université Paris Saclay (COMUE); 2018.
94. Shi T, Xie L, Gu L, Zhu J. Why Sn doping significantly enhances the dielectric properties of Ba(Ti_{1-x}Sn_x)O₃. *Sci Rep*. 2015;5:8606. <https://doi.org/10.1038/srep08606>
95. Dornelas RGF, Silva AC, Garcia JE, Guerra JDS. Features of the structural and dielectric properties in BaTi_{1-x}Sn_xO₃ ferroelectric ceramics. *Ferroelectrics*. 2023;611:84–92. <https://doi.org/10.1080/00150193.2023.2201772>
96. Roy PK, Kumaravelu TA, Roy C, Nga TTT, Chen J-L, Dong C-L, et al. Synergistic contributions of the poling field-induced changes in local structure on the piezoelectric properties of modified BaTiO₃ system. *J Phys D: Appl Phys*. 2025;58:035307. <https://doi.org/10.1088/1361-6463/ad835c>
97. Hennings D. Barium titanate based ceramic materials for dielectric use. *Int J Hig Technol Ceram*. 1987;3:91–111. [https://doi.org/10.1016/0267-3762\(87\)90031-2](https://doi.org/10.1016/0267-3762(87)90031-2)
98. Van Santen JH, Jonker GH. Effect of temperature on the permittivity of barium titanate. *Nature*. 1947;159:333–34. <https://doi.org/10.1038/159333a0>
99. Hollenstein E, Damjanovic D, Setter N. Temperature stability of the piezoelectric properties of Li-modified KNN ceramics. *J Eur Ceram Soc*. 2007;27:4093–97. <https://doi.org/10.1016/j.jeurceramsoc.2007.02.100>
100. Liu W, Ren X. Large piezoelectric effect in Pb-free ceramics. *Phys Rev Lett*. 2009;103:257602. <https://doi.org/10.1103/PhysRevLett.103.257602>
101. Quattropiani A, Makhort AS, Rastei MV, Versini G, Schmerber G, Barre S, et al. Tuning photovoltaic response in Bi₂FeCrO₆ films by ferroelectric poling. *Nanoscale*. 2018;10:13761–66. <https://doi.org/10.1039/C8NR03137A>
102. Dong W, Guo Y, Guo B, Liu H, Li H, Liu H. Photovoltaic properties of BiFeO₃ thin film capacitors by using Al-doped zinc oxide as top electrode. *Mater Lett*. 2013;91:359–61. <https://doi.org/10.1016/j.matlet.2012.10.031>
103. Matsuo H, Noguchi Y, Miyayama M. Gap-state engineering of visible-light-active ferroelectrics for photovoltaic applications. *Nat Commun*. 2017;8:207. <https://doi.org/10.1038/s41467-017-00245-9>
104. Wieder HH. Electrical behavior of barium titanate single crystals at low temperatures. *Phys Rev*. 1955;99:1161–65. <https://doi.org/10.1103/PhysRev.99.1161>
105. Tan Y, Zhang J, Wu Y, Wang C, Koval V, Shi B, et al. Unfolding grain size effects in barium titanate ferroelectric ceramics. *Sci Rep*. 2015;5:9953. <https://doi.org/10.1038/srep09953>
106. Arlt G. The influence of microstructure on the properties of ferroelectric ceramics. *Ferroelectrics*. 1990;104:217–27. <https://doi.org/10.1080/00150199008223825>
107. Bévilion É, Chesnaud A, Wang Y, Dezanneau G, Geneste G. Theoretical and experimental study of the structural, dynamical and dielectric properties of perovskite BaSnO₃. *J Phys Condens Matter*. 2008;20:145217. <https://doi.org/10.1088/0953-8984/20/14/145217>
108. Mueller V, Beige H, Abicht H-P. Non-Debye dielectric dispersion of barium titanate stannate in the relaxor and diffuse phase-transition state. *Appl Phys Lett*. 2004;84:1341–43. <https://doi.org/10.1063/1.1649820>
109. Damjanovic D, Demartin M. Contribution of the irreversible displacement of domain walls to the piezoelectric effect in barium titanate and lead zirconate titanate ceramics. *J Phys Condens Matter*. 1997;9:4943–53. <https://doi.org/10.1088/0953-8984/9/23/018>
110. Kaeswurm B, Schader FH, Webber KG. Ferroelectric, ferroelastic, piezoelectric, and dielectric properties of lead zirconate titanate from –150°C to 350°C. *Ceram Int*. 2018;44:2358–63. <https://doi.org/10.1016/j.ceramint.2017.10.204>
111. Franzbach DJ, Seo Y-H, Studer AJ, Zhang Y, Glaum J, Daniels JE, et al. Electric-field-induced phase transitions in co-doped Pb(Zr_{1-x}Ti_x)O₃ at the morphotropic phase boundary. *Sci Technol Adv Mater*. 2014;15:015010. <https://doi.org/10.1088/1468-6996/15/1/015010>
112. Lei C, Bokov AA, Ye Z-G. Relaxor behavior in Ba(Ti_{0.72}Sn_{0.28})O₃ solid solution. *Ferroelectrics*. 2006;339:129–36. <https://doi.org/10.1080/00150190600738113>
113. Surampalli A, Schiesaro I, Corsi P, Meneghini C, Sathe VG, Sagdeo A, et al. Evidence of structural modifications in the region around the broad dielectric maxima in the 30% Sn-doped barium titanate relaxor. *Phys Rev B*. 2019;100:134104. <https://doi.org/10.1103/PhysRevB.100.134104>
114. Merselmiz S, Hanani Z, Mezzane D, Spreitzer M, Bradeško A, Fabijan D, et al. High energy storage efficiency and large electrocaloric effect in lead-free BaTi_{0.89}Sn_{0.11}O₃ ceramic. *Ceram Int*. 2020;46:23867–76. <https://doi.org/10.1016/j.ceramint.2020.06.163>
115. Kacem H, Dhahri A, Sassi Z, Seveyrat L, Lebrun L, Perrin V, et al. Relaxor characteristics and pyroelectric energy harvesting performance of BaTi_{0.91}Sn_{0.09}O₃ ceramic. *J Alloys Compd*. 2021;872:159699. <https://doi.org/10.1016/j.jallcom.2021.159699>
116. Luo Z, Zhang D, Liu Y, Zhou D, Yao Y, Liu C, et al. Enhanced electrocaloric effect in lead-free BaTi_{1-x}Sn_xO₃ ceramics near room temperature. *Appl Phys Lett*. 2014;105:102904. <https://doi.org/10.1063/1.4895615>
117. Yasuda N, Hidehiro Ohwa HO, Shigeto Asano SA. Dielectric properties and phase transitions of Ba(Ti_{1-x}Sn_x)O₃ solid solution. *Jpn J Appl Phys*. 1996;35:5099. <https://doi.org/10.1143/JJAP.35.5099>
118. Picht G, Webber KG, Zhang Y, Kungl H, Damjanovic D, Hoffmann MJ. Critical mechanical and electrical transition

- behavior of BaTiO₃: the observation of mechanical double loop behavior. *J Appl Phys.* 2012;112:124101. <https://doi.org/10.1063/1.4767059>
119. Mitoseriu L, Curecheriu LP. Nanostructured barium titanate ceramics: intrinsic versus extrinsic size effects. In: *Nanoscale ferroelectrics and multiferroics*. John Wiley & Sons, Ltd; 2016, p. 473–511. <https://doi.org/10.1002/9781118935743.ch15>
 120. Mitoseriu L, Tura V, Ricinschi D, Harnagea C. Grain size dependence of the Rayleigh coefficients in barium titanate ceramics. *Ferroelectrics.* 2000;240:1317–24. <https://doi.org/10.1080/00150190008227952>
 121. Liu Q, Zhang Y, Gao J, Zhou Z, Yang D, Lee K-Y, et al. Practical high-performance lead-free piezoelectrics: structural flexibility beyond utilizing multiphase coexistence. *Natl Sci Rev.* 2020;7:355–65. <https://doi.org/10.1093/nsr/nwz167>
 122. Atito IA, Shaban HT, Salem A, Ezzeldien M, Mahmoud AE. Sub-switching domain effect for analysis the non-linear dielectric behavior of (K_{0.49}Na_{0.49}Li_{0.02}) (Nb_{0.98}Sb_{0.02})O₃ ceramic based on Rayleigh model. *J Korean Ceram Soc.* 2022;59:705–14. <https://doi.org/10.1007/s43207-022-00218-9>
 123. Peng B, Yue Z, Li L. Evaluation of domain wall motion during polymorphic phase transition in (K, Na)NbO₃-based piezoelectric ceramics by nonlinear response measurements. *J Appl Phys.* 2011;109:054107. <https://doi.org/10.1063/1.3553857>

SUPPORTING INFORMATION

Additional supporting information can be found online in the Supporting Information section at the end of this article.

How to cite this article: Kraft V, Eckstein UR, Kuhfuß M, Khansur NH, Marlton FP, Mullens B, et al. Temperature-dependent electromechanical response of BaTi_{1-x}Sn_xO₃: Analysis of reversible and irreversible contributions. *J Am Ceram Soc.* 2025;e70233. <https://doi.org/10.1111/jace.70233>